



Facile synthesis of defect induced $\text{CeO}_2/\text{MIL}-53(\text{Fe})$ nanocatalyst: Strategically switching the charge transfer dynamics for remarkable enhancement of photocatalytic Bisphenol A degradation and H_2 evolution

Ugrabadi Sahoo ^a, Samarjit Pattnayak ^a, Shubhalaxmi Choudhury ^a, Pragnyashree Aparajita ^a, Dillip Kumar Pradhan ^b, Garudadhwaj Hota ^{a,*},¹

^a Department of Chemistry, National Institute of Technology, Rourkela 769008, Odisha, India

^b Department of Physics and Astronomy, National Institute of Technology, Rourkela, Odisha 769008, India



ARTICLE INFO

Keywords:

Oxygen vacancy
Switching of Charge transfer
Photocatalysis
Bisphenol A
 H_2 evolution

ABSTRACT

This work reports the fabrication of heterojunction between defect induced CeO_2 and iron based metal organic framework (MIL-53). A simple chemical redox etching methodology was adopted to narrow the band gap of pristine CeO_2 through oxygen vacancy engineering. The photocatalytic efficacy of defect induced $\text{CeO}_2/\text{MIL}-53$ (MCO-X) heterojunction was studied in Bisphenol A (BPA) breakdown and photocatalytic hydrogen generation from water splitting. The significantly improved photocatalytic application of MCO-X heterojunction could be attributed to the switching of charge dynamics mechanism from Type-I to Type-II due to defect formation in the pristine CeO_2 . The optimal photocatalyst (MCO-30) displayed the highest photocatalytic BPA degradation with rate constant (0.045 min^{-1}) and H_2 evolution ($3286.2 \text{ } \mu\text{mol.h}^{-1} \cdot \text{g}^{-1}$) respectively. This study provides a comprehensive analysis on how defect in pristine CeO_2 in MCO-X heterojunction can switch the charge transfer mechanism from Type-I to Type-II to achieve remarkable visible light harnessing capacity and photocatalytic activity.

1. Introduction

One of the major global concerns that have drawn a lot of attention from the scientific community is water contamination brought on by persistent micropollutants and the prospect of global energy crisis [1–4]. The harmful micropollutant bisphenol A (BPA) has endocrine-disrupting qualities and interferes with human hormone action, leading to cancer, anomalies in the reproductive system, and other systemic illnesses [5,6]. BPA has been recognized as a possible aquatic hazard as a result of its extensive use in polymer industries and subsequent environmental discharge [7]. In the search for green and sustainable energy and decontamination methods for reducing environmental pollution and addressing the global energy crisis, the photocatalytic method is by far the most significant technique to address these complex issues [8–10]. The photocatalytic technique differs from conventional methods, in that it uses renewable energy and is biocompatible and more efficient. As a potential alternative to current energy sources, the photocatalytic H_2 generation from the splitting of water on the surface of a semiconductor

is being studied extensively [11,12]. In recent years, many commercial applications, such as optical display technology, photocatalysis, corrosion prevention, three-way vehicle catalytic converters, solar energy devices and electrocatalytic application have drawn significant interest in the chemistry that takes place at the surfaces of metal oxides. CeO_2 is a crucial rare earth oxide among the metal oxides that has received a lot of interest for usage in catalysis, sensors, fuel cells, and biological applications [13–17]. The usage CeO_2 as an electronic material for logic operations and as a photocatalyst is constrained due to its broad band gap energy (2.7–3.4 eV) [18]. A well-known technique for adjusting the band structure and dominant carrier type for electrical and optical applications is chemical functionalization of CeO_2 [19]. Yet, very few research have examined the extent to which nonmetals and metals may be doped to tune the band gap. A very rare studies demonstrated that the chemical etching can be utilized for the fabrication of defect induced CeO_2 in order to achieve the desired band gap for significant photocatalytic applications [20]. Chemical etching is a potent post-processing technique that may be used to alter the morphologies of materials while

* Corresponding author.

E-mail address: garud@nitrk.ac.in (G. Hota).

¹ orcid.org/0000-0001-8267-0443

maintaining or improving the qualities of target materials. After being subjected to chemical etching using NaBH_4 as the reducing agent, spindle-shaped CeO_2 underwent morphology evolution as well as improvements in their specific surface areas, oxygen vacancy concentrations, and surface Ce^{3+} concentrations [20]. Due to the reversible $\text{Ce}^{3+}/\text{Ce}^{4+}$ redox pair, the abundance of surface oxygen vacancies, CeO_2 , a commonly utilized as rare earth oxide, has been significantly investigated as a catalytically effective species, supporter, and help in the field of photocatalysis [21].

Recently, the scientific community has become much more interested in development of metal-organic frameworks (MOFs) photocatalyst. MOFs are extremely crystalline substances created by the self-assembly of organic ligands, metal ions, or cluster of metals [22]. MOFs are regarded as a favorable class of photocatalyst materials as they possess high crystallinity, capacity to tune the bandgap in heterostructures, customizable porous structure, high specific surface area, capacity to tolerate the functional group, etc. Recent developments have seen the use of MOF-based materials in critical fields such as adsorption of gas, drug delivery, chemical sensing, and heterogeneous catalysis [23–26]. The organic linkers in MOFs operate as an antenna for electromagnetic radiation interaction, whilst the metal clusters act as quantum dots for light harvesting. Several MOFs, such as MIL-53(Fe), MIL-125(Ti), UIO-66(Zr), and HKUST-1, have recently been proven to be excellent photocatalysts for the oxidation of oxygen, reduction of carbon dioxide, oxidation of hydrocarbons, and photodegradation of hazardous chemicals, respectively [27], [28], [29], [30]. Fe-based MOF (MIL-53) has a considerable influence on the scientific community among MOF-based photocatalysts because of its structural stability, significant crystallinity, ability to control the bandgap in hybrid composites, and amazing ability to harness light. However, MIL-53(Fe) has a high rate of photoinduced electron (e⁻) and hole (h⁺) pair recombination, leads to poor photocatalytic efficiency [31]. In order to overcome that, in recent years there have been attempts to create MIL-53 based heterostructure to enhance the photocatalytic effectiveness of MIL-53 (Fe). Tetracycline hydrochloride (TCH), Bisphenol A (BPA), Rhodamine B (RhB), and other organic pollutants have all been photo-degraded extensively using functional MIL-53. Moreover, MIL-53 has also been used in photocatalytic water splitting to provide clean, sustainable energy to address the global energy crisis.

Considering these above points, in this current study we have synthesized defect induced CeO_2 by simple chemical etching process. We show that chemically etching CeO_2 powders with NaBH_4 may change the surface structure and control the band gap of CeO_2 by generating a variety of localized energy levels. The chemical etching process resulted in the formation of oxygen vacancy in CeO_2 without affecting the crystal structure. Compared to pure CeO_2 (p- CeO_2), the defect-induced CeO_2 (d- CeO_2) material exhibited better optoelectronic properties. The defect induced CeO_2 (d- CeO_2) are subsequently integrated with MIL-53 (Fe) MOF to fabricate d- CeO_2 /MIL-53 (MCO) heterostructure composites. The significant photocatalytic effectiveness of the as fabricated heterostructure has been investigated for Bisphenol A degradation and photocatalytic H_2 evolution under visible light irradiation.

2. Experimental section

The substances that were employed to create the photocatalyst materials are listed in the [supplemental information](#) file.

2.1. Synthesis of pristine CeO_2 (p- CeO_2)

A facile hydrothermal synthetic approach has been adopted for the fabrication of spindle-shaped pristine CeO_2 [32]. 44 mL of 0.1 M $\text{Ce}(\text{NO}_3)_3 \cdot 6 \text{H}_2\text{O}$ and 8 mL of 6.0 M NaOH solutions were combined first, and the combined solution was then rapidly stirred for 0.5 h. A 100 mL Teflon liner was then filled with the mixed solution, and the Teflon liner was placed inside a stainless steel autoclave. Finally, the autoclave was

brought to temperature at 150 °C and kept there for 12 h. After filtering, washing with ethanol and DI water, and drying in a 60 °C oven for 12 h, spindle-shaped pure CeO_2 powder was obtained.

2.2. Synthesis of defect induced CeO_2 nanostructures (d- CeO_2)

The obtained CeO_2 powder underwent a chemical redox etching treatment [20]. 500 mg of freshly prepared CeO_2 powder were dissolved 500 mL of deionized water that has been irradiated with ultrasonic waves. After adding 6 wt percentage of NaBH_4 , the CeO_2 /water solution was agitated for 12 h on a magnetic stirrer hotplate. The samples were then put into a Teflon liner with a 100 mL capacity, which was then put into an autoclave made of stainless steel for 150 °C for 12 h. The materials were subsequently obtained by centrifugation followed by washing with ethanol and DI water and designated as d- CeO_2 [Scheme 1](#) and [3](#).

2.3. Synthesis of MIL-53 (Fe)

MIL-53(Fe) is synthesized by the solvothermal process as per the reported literature [31]. In a archetypal synthetic method 1.66 g of 1,4 BDC, 2.703 g of $\text{FeCl}_3 \cdot 6 \text{H}_2\text{O}$ were dissolved in 56 mL DMF followed by strongly stirring for 30 min at room temperature till the Teflon liner and heated at 150 °C for 24 h in a solvothermal treatment. The solution was then cooled to ambient temperature and centrifuged three times each with DMF and ethanol. The yellowish sample was taken and dried in a 60 °C oven for the entire night.

2.4. Synthesis of d- CeO_2 @ MIL-53 (MCO-X) heterostructure

In a typical solvothermal approach 2.703 g of $\text{FeCl}_3 \cdot 6 \text{H}_2\text{O}$ and 1.66 g of 1, 4-BDC with different weight percentages of defect induced CeO_2 (10, 20, 30 and 40 wt% i.e., 0.436, 0.872, 1.308, 1.745 g respectively) were added along with 56 mL DMF. To obtain a translucent and clear solution, the mixture was rapidly agitated for 30 min. Then the solution was transferred to a 100 mL autoclave for solvothermal treatment for 150 °C for 24 h. Then the samples were collected by following centrifugation, and drying the samples at 60 °C for 12 h and marked these samples as MCO-10, MCO-20, MCO-30, and MCO-40. [Scheme 2](#) represents the schematic synthetic route of MCO-30 heterostructure.

2.5. Characterization technique

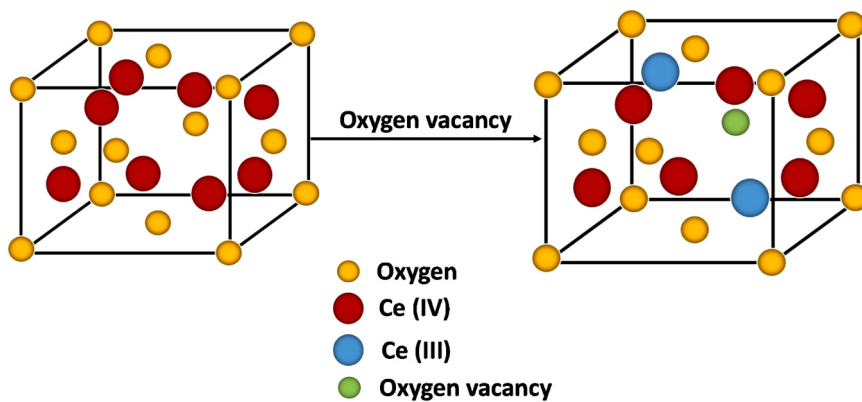
An extensive explanation of the tools used for materials characterization is illustrated in the [supplemental information](#) file.

2.6. Electrochemical measurements

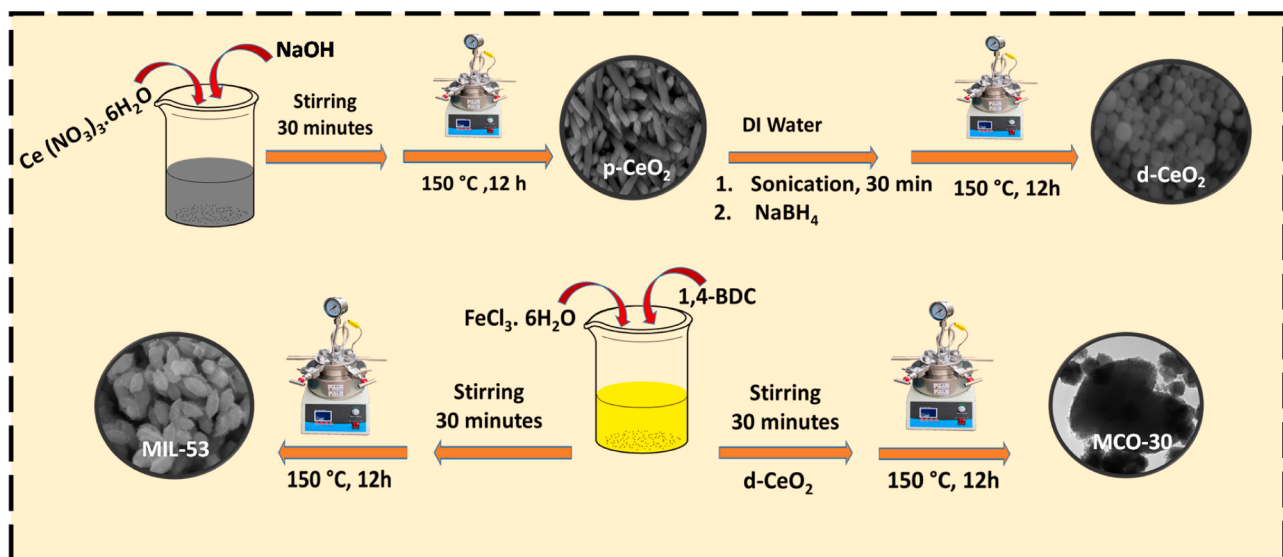
Measurements for the instantaneous photocurrent, Mott-Schottky, and electrochemical impedance spectroscopy (EIS) analyses were made using an electrochemical work-station (CHI660C Apparatuses). The working electrode is the slurry photo catalyst mixture that has been coated on FTO glass, whereas the counter electrode is Pt foil and (Ag/AgCl) serves as the reference electrode. A 300 W Xe lamp works as the light source. The reported literature was used to guide the fabrication of the electrodes for the aforementioned tests [33]. In the experiment, 0.5 M Na_2SO_4 was used as the electrolyte for the measurements of the photocurrent at pH (6.8).

2.7. Photocatalytic investigation

The degradation of Bisphenol A (BPA) and photocatalytic production of hydrogen from water splitting were examined to determine the photocatalytic effectiveness of the synthesized nanocomposite materials.



Scheme 1. Schematic model illustrating change in crystalline structure of CeO_2 after the formation of Ce^{+3} due to oxygen vacancy.



Scheme 2. Schematic route of synthesis of MCO-30 heterostructure.

2.7.1. Photocatalytic degradation of Bisphenol A

An investigation on the photocatalytic breakdown of BPA was investigated using a 250 W visible light source. For this procedure, a photocatalytic reactor was used that was well-maintained with a cool water flow to safeguard the longevity of the reactor. 100 mL of a 10 ppm BPA solution and 0.1 g of photocatalyst were introduced to the reactor. To keep the adsorption-desorption equilibrium, the solution was then held in the dark while being stirred for an hour. A visible light source of 250 W was then irradiated. The catalyst was removed from the sample solution by centrifugation after each segment of 10 min, and the absorbance of the homogeneous solution was then characterized using a Xin Mao 723 pcs UV-Visible spectrophotometer. Experiments on the breakdown of BPA using various synthesized photocatalysts were conducted for the purpose of comparative studies. The percentage of deterioration was determined at the conclusion of each trial using the provided equation.

$$\% \text{ of Degradation} = \left(\frac{C_0 - C_t}{C_0} \right) \times 100 \quad (1)$$

Where C_0 = initial concentration of BPA, C_t = concentration of BPA at time "t".

2.7.2. Photocatalytic hydrogen evolution from water splitting

The as-prepared materials with methanol serving as a trapping agent were used to investigate the photocatalytic hydrogen production from

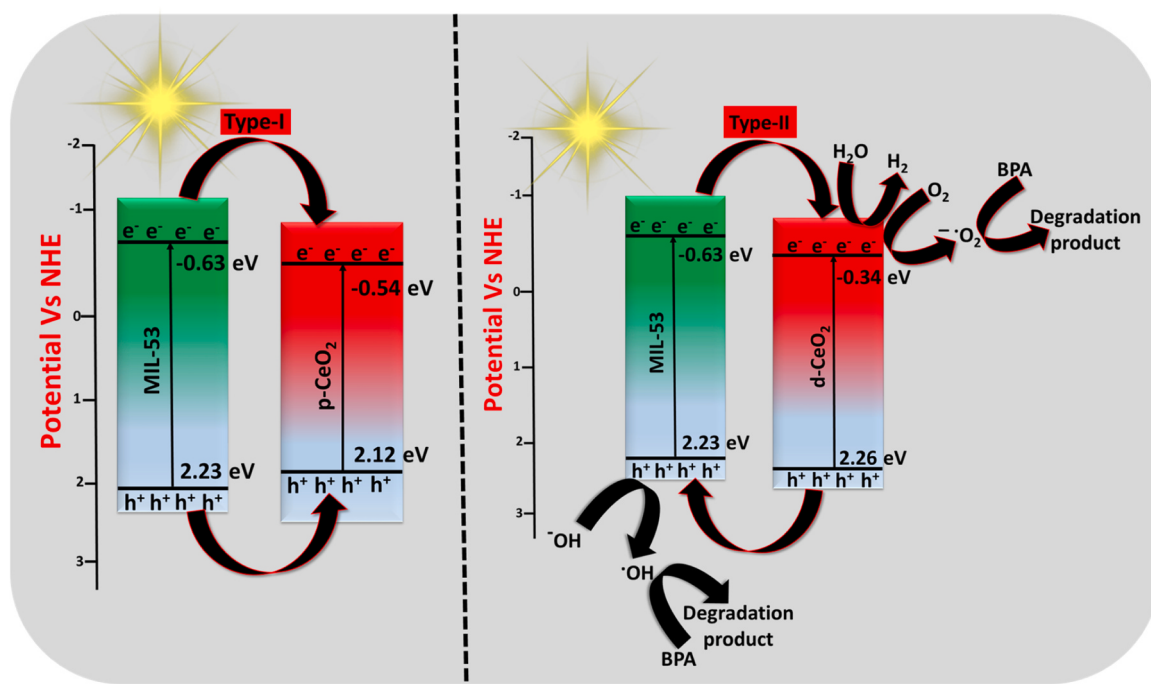
water splitting. A quartz glass photoreactor with a running gas circulation system was used for this technique. In a representative experiment, 80 milligrams of photocatalyst was dissolved in 80 milliliter of aqueous methanol at a 10 vol% concentration. The whole solution was sonicated for 30 min, then constantly stirred for 30 min with N_2 present to maintain the atmosphere of the photoreactor inert. The catalytic solution was then lit with a 250 W visible light source lamp using a TCD detector and a NUCON 5765 type GC, the reaction was run constantly for 4 h while measuring the amount of H_2 gas produced at various time points. The efficiency of hydrogen energy exchange was calculated using the following algorithm. [34].

$$\text{Conversion efficiency}(\%) = \frac{\text{Stored chemical energy}}{\text{Energy of incident light}} \times 100 \quad (2)$$

3. Results and discussions

3.1. Characterization of photocatalysts

To get the information regarding crystallinity and phase purity of the synthesized materials, XRD analysis was carried out (Fig. 1(a)). The XRD array of pristine CeO_2 (p- CeO_2) could be assigned to the fluorite phase of CeO_2 (JCPDS CARD NO-81 –0792). The peaks at 28.6, 33.1, 47.5, 56.3, 59.1, 69.4, 76.7, 79.0 degrees were allocated to the (111), (200), (220), (311), (222), (400), (331), (420) miller planes respectively [18]. There



Scheme 3. Potential switch-off mechanism for charge transfer dynamics for BPA degradation and H_2 evolution in MCO-30 heterostructure.

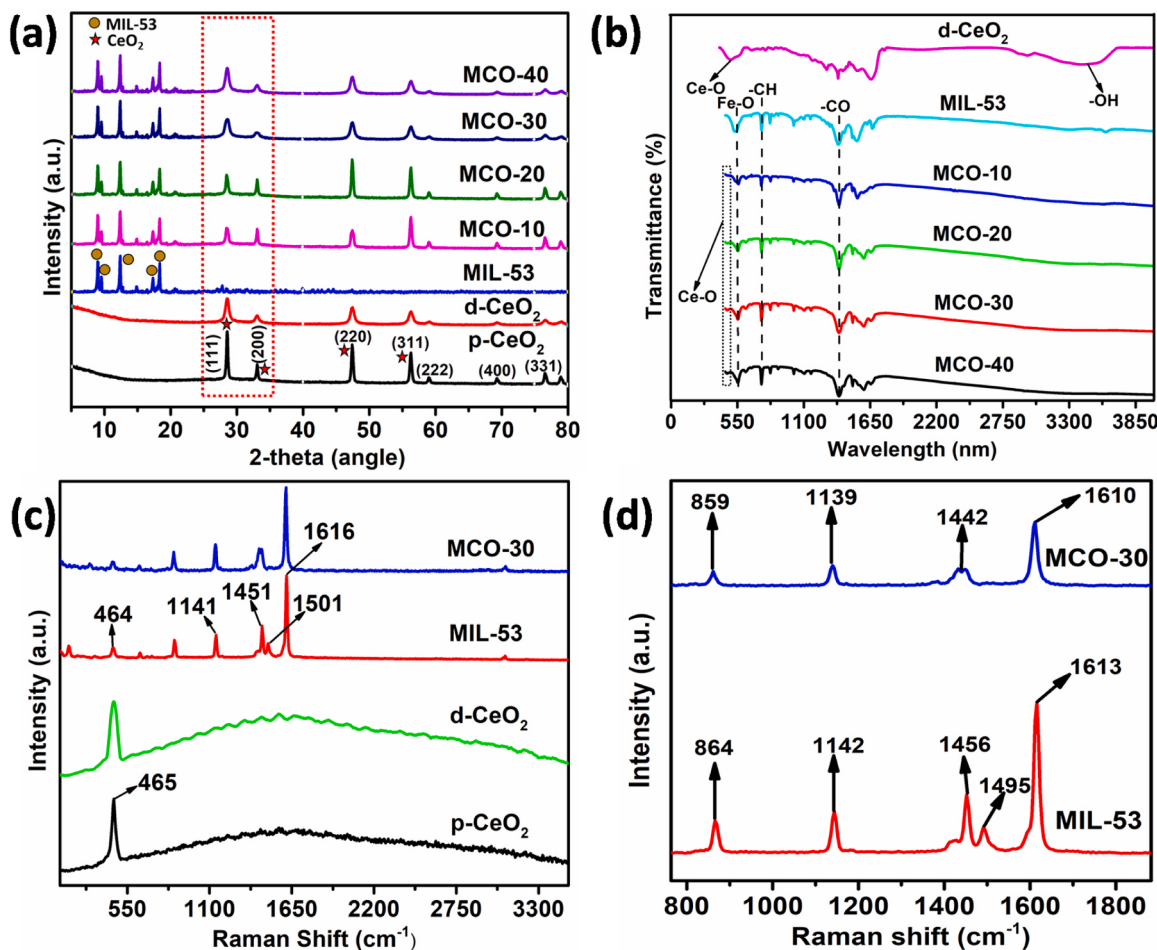


Fig. 1. (a) XRD pattern of p-CeO₂, d-CeO₂, MIL-53, and MCO-X heterostructure, (b) FTIR analysis of d-CeO₂, MIL-53, and MCO-X heterostructure, (c) Raman spectra of pristine p-CeO₂, d-CeO₂, MIL-53, and MCO-30 heterostructure (d) Raman spectra (enlarged version) of MIL-53 and MCO-30.

was no clear evidence of crystalline Ce_2O_3 or $\text{Ce}(\text{OH})_3$. There are no further impurity peaks visible, demonstrating the excellent pureness and solitary phase crystallinity of the CeO_2 samples. The XRD pattern of defect induced CeO_2 (d- CeO_2) were similar to p- CeO_2 with some minor alteration in the peak intensities and peak broadening. This demonstrates that, despite the fact that the peak intensities have decreased, the fundamental fluorite cubic structure of CeO_2 has not altered even after the defect formation. A very small margin of peak shift was observed in d- CeO_2 (Fig. S1), which could be ascribed to oxygen vacancies, defects and formation of Ce^{+3} ion that contribute in the development of internal strain [18]. The reduction in crystallite size and generated microstrain may be the cause of this peak broadening in d- CeO_2 [35]. The crystallite size and microstrain can be calculated by using the Williamson-Hall equation which mentioned below

$$\beta \cos \theta = 4\epsilon \sin \theta + \frac{k\lambda}{D} \quad (3)$$

Where β = full width at half maximum, θ = diffraction angle, ϵ = microstrain, k = constant (0.9), λ = X-ray wavelength of $\text{Cu K}\alpha$, D = average crystallite size.

Williamson-Hall plot is constructed by plotting $4\sin\theta$ along x-axis and $\beta \cos\theta$ along y-axis. The obtained plot is linearly fitted and the crystallite size and microstrain are estimated from the intercept and slope of the curve, respectively. In Fig. S1 (b&c), the Williamson-Hall plot of p- CeO_2 and d- CeO_2 has been demonstrated, and Table 1 lists the findings. The findings further demonstrate that d- CeO_2 exhibits decrease in crystallite size and increase in microstrain which favour the lattice relaxation. The diffraction peaks in the range of 7–35° for MIL-53 are exactly in agreement with the previously reported literature. The most significant peaks at 9.12°, 17.64°, 18.38°, 25.41°, and 27.27° are in-line with the reported literature suggesting the efficacious fabrication of MIL-53 [36]. The existence of all the major crystalline phases of CeO_2 and MIL-53 in the XRD pattern of MCO-X heterostructure clearly suggests the successful fabrication of MCO-X heterostructure.

To investigate the detailed analysis of chemical bonds and functional groups of the synthesized materials, FTIR studies were done from 4000 to 400 cm^{-1} (Fig. 1(b)). The peak at 482 cm^{-1} in the FTIR spectrum of p- CeO_2 indicates to the presence of metal-oxygen bond (Ce-O stretching). The band observed at 3426 cm^{-1} is consigned to the vibration mode of O-H stretching of adsorbed water [37]. The FTIR spectrum of defect induced CeO_2 (d- CeO_2) were alike to p- CeO_2 except for a little variation in peak intensities and peak broadening (Fig S2). This may be due to the existence of oxygen vacancy and Ce^{+3} ions in CeO_2 [38]. The FTIR spectrum of MIL-53 shows two sharp bands at 1537 cm^{-1} and 1387 cm^{-1} corresponding to asymmetric (-CO) stretching and symmetric (-CO) stretching of -COO in the dicarboxylate linker respectively [39]. In pure MIL-53 and its composites, the intense peak at 750 cm^{-1} is ascribed to the stretching vibration -CH of terephthalic ring. According to previously published literature, a sharp peak at 539 cm^{-1} is ascribed to Fe-O vibrations that reflect the iron-carboxylate bonding [40]. The presence of both Ce-O stretching frequency and the Fe-O vibration band in the MCO-X composite at 482 cm^{-1} and 500 cm^{-1} , respectively, indicating that MIL-53 and d- CeO_2 successfully interacted to generate the MCO-X heterostructure.

The intrinsic microstructural characteristics of p- CeO_2 , d- CeO_2 , MIL-53, and MCO-30 heterostructure were well explored via Raman scattering technique (Fig. 1(c & d)). A strong and prominent peak observed at approximately 465 cm^{-1} for both p- CeO_2 and d- CeO_2 which was

allocated to the F2g Raman active symmetrical stretching mode of CeO_2 [19]. However, the peak broadening was observed for d- CeO_2 at 465 cm^{-1} which was ascribed to morphology change, strain, dislocations in the crystal, and the formation of Ce^{+3} ion [18]. A prominent peak at 464 cm^{-1} in the Raman spectra indicates the presence of a gamma bond between Fe and Oxo in MIL-53 (Fig. 1(c)) [41]. The peak at 1141 cm^{-1} designates the link between two sp^2 hybridized carbon atoms of the benzene ring and carboxylate groups. The existence of asymmetric (C-O) and symmetric (C-O) of -COO organic linkers is indicated by the peaks at 1451 cm^{-1} and 1501 cm^{-1} in MIL-53, respectively [34]. The typical (C=C) bond of the aromatic cycle is reflected by the sharp and rising prominence peak at 1616 cm^{-1} . The vibrational bands of the H₂BDC ligand dominate the entire Raman spectrum of MIL-53. The Raman spectra of MCO-30 contain all the characteristic peaks of MIL-53 and d- CeO_2 . However, all of the individual peaks of MIL-53 in the MCO-30 composite have been shifted from 864, 1141, 1451, and 1616 cm^{-1} to 859, 1139, 1442, and 1610 cm^{-1} (Fig. 1(d)), suggesting successful interaction of d- CeO_2 with MIL-53 [42].

For the enhanced study regarding the morphology, the as prepared pure and heterostructure materials are analyzed by SEM and TEM. The SEM pattern of p- CeO_2 reveals the homogeneous spindle shaped structure of CeO_2 with length varies from 2 to 3 μm ((Fig. 2(a)). In d- CeO_2 , Ce^{+3} is generated when Ce^{+4} is reduced by the electrons leftover after an oxygen vacancy forms in the lattice. It is observed that reduced Ce^{+3} cations have a larger size (115 pm) than Ce^{+4} (101 pm). The size fluctuation of Ce^{+4} and Ce^{+3} as well as oxygen vacancies cause tension in the lattice and alter the local symmetry of p- CeO_2 . The decrease in particle size that has the ability to produce additional defects and oxygen vacancies is a key factor regulating the intrinsic defect concentration. Defect induced CeO_2 (d- CeO_2) shows spherical morphology as the lattice tends to show wider size expansion to release the internal strain produced by the oxygen vacancy in p- CeO_2 ((Fig. 2(b)) [43,44]. A clear well-shaped hexagonal structure was obtained for MIL-53 with length varies from 1 to 2 μm and breadth 0.5–1 μm ((Fig. 2(c)). The SEM micrograph of MCO-30 heterostructure shows the presence of both hexagonal shaped MIL-53 along with very tiny d- CeO_2 particle uniformly dispersed on the surface of MIL-53 ((Fig. 2(d)). The elemental mapping and EDX survey of MCO-30 suggests all the individual elements are present in an appropriate percentage (Fig S3). These shreds of informations suggest the successful fabrication of MCO-30 heterostructure.

The TEM analysis of d- CeO_2 shows spherical shaped particle with diameter approximately 20 nm (Fig. 3(a)). TEM micrograph of MCO-30 shows the presence of both hexagonal shaped MIL-53 having length about 200 nm and spherical shaped d- CeO_2 (Fig. 3(b and c)). A clear interfacial contact in between MIL-53 and d- CeO_2 can be seen from the TEM micrograph of MCO-30. HRTEM micrograph shows interplanar distance of 0.310 and 0.267 nm which corresponds to the (111) and (200) miller plane of CeO_2 respectively (JCPDS card no- 81 –0792) (Fig. 3(e)). The obtained HRTEM results are well in line with XRD results. No obvious HRTEM fringe of MIL-53 was found [39]. The SAED pattern of MCO-30 revealed two bright and clear rings that were clearly visible, which also corresponds to the (111) and (200) miller plane of CeO_2 (Fig. 3(d)). The above shreds of evidences clearly suggest the successful fabrication of MCO-30 heterostructure.

The specific surface area of the synthesized p- CeO_2 , d- CeO_2 , MIL-53, and the MCO-30 heterostructure were evaluated by the N_2 sorption analysis. The isotherms of adsorption-desorption and pore size distributions are depicted in Fig. 4(a & b), and the findings are precisely abridged in Table 2. The specific surface area of MIL-53 is 271.8 $\text{m}^2\cdot\text{g}^{-1}$ obtained from multipoint BET analysis. A H_3 type of hysteresis loop having surface area of 132 and 86.6 $\text{m}^2\cdot\text{g}^{-1}$ was displayed by p- CeO_2 and d- CeO_2 respectively. The pore diameter and pore volume of d- CeO_2 (2.975 nm and 0.063 cc g^{-1}) is comparatively more as compared to p- CeO_2 (2.968 nm and 0.060 cc g^{-1}), which may be due to the defect

Table 1

The calculated crystallite size and microstrain value of p- CeO_2 and d- CeO_2 by Williamson-Hall plot.

Sample	Crystallite size (D) in nm	Macrostrain (ϵ) $\times 10^{-3}$
p- CeO_2	37.03	0.0007
d- CeO_2	27.95	0.002

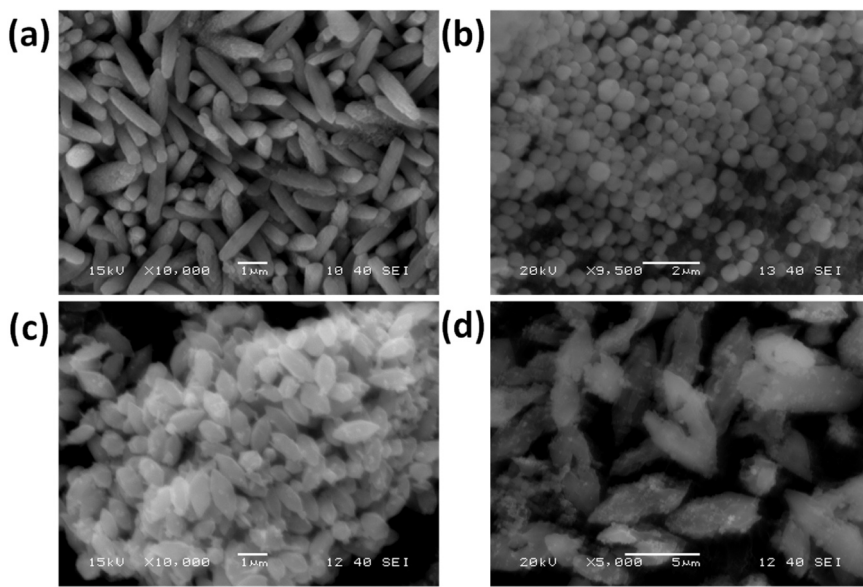


Fig. 2. SEM images of (a) p-CeO₂, (b) d-CeO₂, (c) MIL-53, and (d) MCO-30.

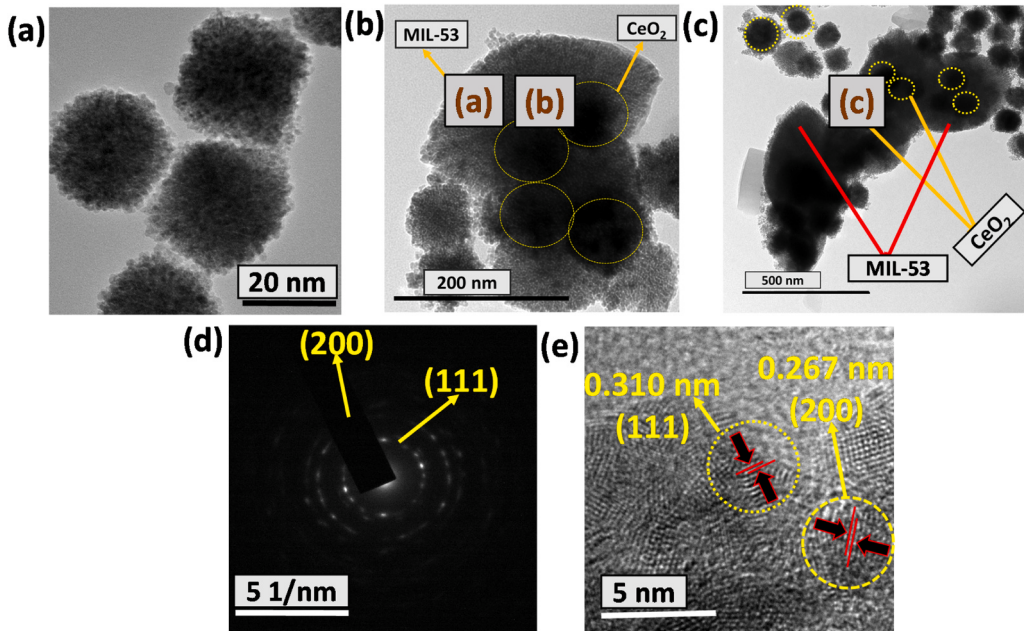


Fig. 3. TEM images of (a) d-CeO₂, (b & c) MCO-30, (d) SAED pattern of MCO-30 and (e) HRTEM of MCO-30.

induction in pristine CeO₂ (Table 1). The BJH pore size distribution displayed the pore diameter of MCO-30 is 3.121 nm which was relatively low as compared to MIL-53 (3.316 nm), indicating the surface integrity of d-CeO₂ particle on MIL-53 surface.

XPS survey spectrum of MCO-30 reveals the coexistence of C, O, Fe and Ce elements (Fig. 5(a)). In Fig. 5(b), two bands at energies of 284.03 eV and 288.4 eV, respectively, in the C 1 S XPS spectrum show the sp^2 hybridized C-C bond and the C=O bond in the H₂BDC ligand [45]. Two peaks are shown by the XPS spectrum of O 1 s (Fig. 5(c)) at 529.9 eV and 531.6 eV attributing to the Fe-O bond of MIL-53 and oxygen constituent of carboxylate group of H₂BDC ligand respectively [31]. The lattice oxygen of CeO₂ shows a typical peak at 529.4 eV [46]. The Fe^{III} oxidation state of the MIL-53 framework is represented by two peaks in the deconvoluted spectrum of Fe 2p with energies of 710.11 eV and 723.86 eV, respectively [31]. Fig. 5(e) shows the Ce 3d spectra and

associated peak fitting findings. Four pairs of spin-orbit doublets are represented by the eight peaks connected to 3d electrons of Ce. The peak labelled at 916.9, 907.4, 901.4, 898.4, 889.1 and 882.7 eV refers to the 3d_{3/2} and 3d_{5/2} respectively, which are the characteristics peaks of Ce⁺⁴ 3d final states where as peaks at 903.4 and 885.9 eV corresponds to the 3d_{3/2} and 3d_{5/2}, respectively, and are present for Ce³⁺ 3d final states [46]. The presence of both Ce⁺⁴ and Ce⁺³ ion indicates to the existence of oxygen vacancy induced CeO₂ (d-CeO₂) in the MCO-30 heterostructure.

The EPR investigation provides more evidence regarding defect in CeO₂. Atomic oxygen defects in the d-CeO₂ crystal lattice are what cause an EPR signal to appear at $g = 2.003$. (Fig. S4) [47]. Since there are no EPR spectra for pure cerium oxide (p-CeO₂), it is likely that oxygen vacancies are only created during the hydrothermal synthesis of NaBH₄ treated with CeO₂. This results are also in line with the XRD, and

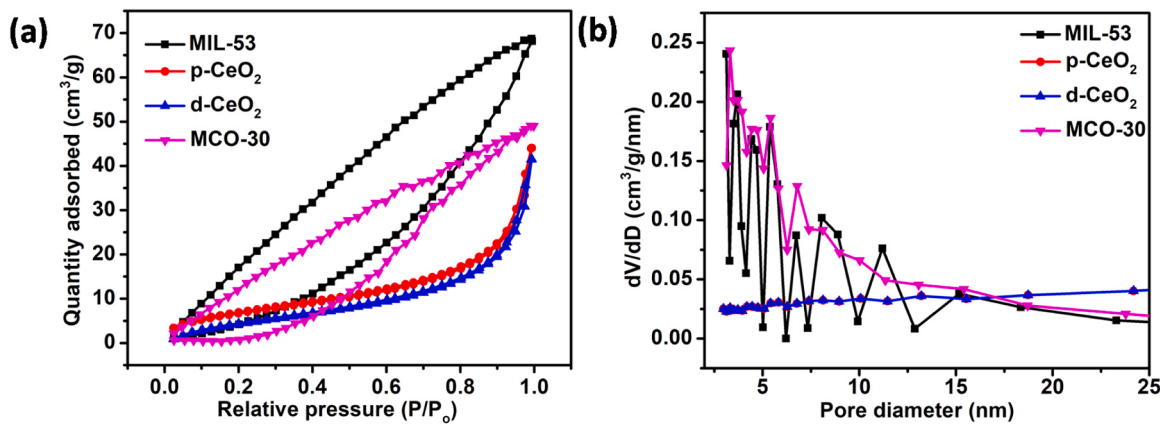


Fig. 4. (a) BET specific surface area analysis of MIL-53, p-CeO₂, d-CeO₂ and MCO-30 (b) BJH pore size distribution of MIL-53, p-CeO₂, d-CeO₂ and MCO-30.

Table 2

BET measurements of the MIL-53, p-CeO₂, d-CeO₂, and MCO-30 composite materials with surface area, pore volume, and typical pore diameter.

Samples	Surface area (m ² g ⁻¹)	Pore volume (cc g ⁻¹)	pore diameter (nm)
MIL-53	271.8	0.091	3.316
p-CeO ₂	132	0.060	2.968
d-CeO ₂	86.6	0.063	2.975
MCO-30	241.5	0.068	3.121

morphology analysis.

4. Optical and electrochemical analysis

For the investigation of optical absorption properties of visible light harvesting efficiency, UV-Visible DRS analysis has been carried out in Fig. 6(a). From the plot, the absorption efficiency of pristine MIL-53 and d-CeO₂ were found to be 433 nm and 476 nm respectively. It's

intriguing that d-CeO₂ has significant absorption efficiency as compared to p-CeO₂ which shows absorption maxima at 441 nm (Fig. S5a); the existence of Ce³⁺ at the grain boundaries has been implicated in the red-shift in wavelength, and raising the abundance of Ce³⁺ causes the decrease in band gap, forming some localized energy states in the band gap. [48]. However, MCO-30 composite shows the absorption maxima at 619 nm. This results shows that MCO-30 composite can be demonstrated as a highly visible light driven photo catalyst that can be eventually used as a potential candidate for the photocatalytic applications.

The following equation was used to examine the optical band gap using data on optical absorption against wave length at the band edge.

$$(\alpha h\nu)^2 = A(h\nu - E_g) \quad (4)$$

By calculating the intercepts of the tangents of the plots of $(\alpha h\nu)^2$ vs. $h\nu$, one may get the band gap energy value. The calculated band gap energy values of MIL-53, and d-CeO₂ were observed to be 2.86 eV and 2.60 eV (Fig. 6(b)) respectively. However, the band gap energy value of p-CeO₂ was obtained to be 2.81 eV (Fig S5b). The resulting lower band

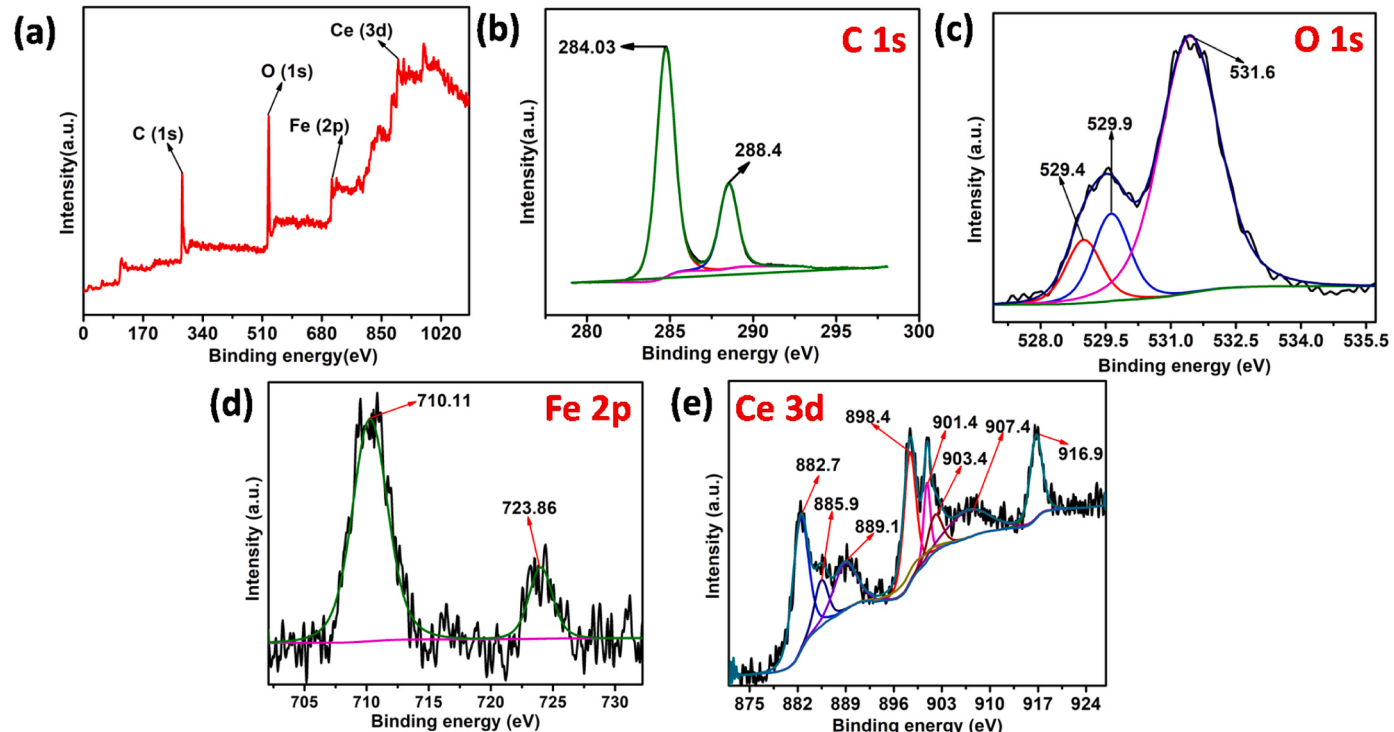


Fig. 5. XPS survey spectra of MCO-30 composite (a), C 1 s spectrum (b), O 1 s spectrum (c), Fe 2p spectrum (d) and Ce 3d spectrum.

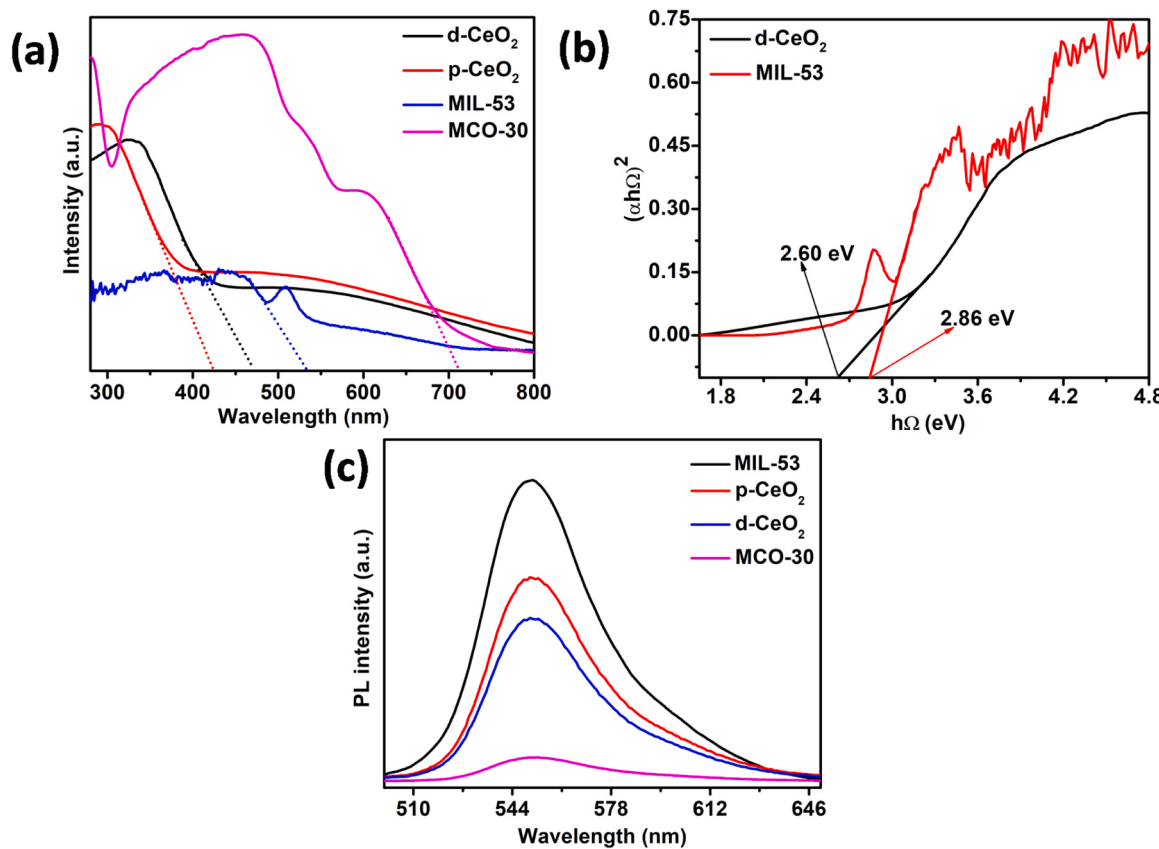


Fig. 6. (a) UV-vis DRS study of MIL-53, p-CeO₂, d-CeO₂ and MCO-30 composite. (b) Tauc's plot of MIL-53 and d-CeO₂ (c) PL emission intensity plot of MIL-53, p-CeO₂, d-CeO₂ and MCO-30 composite.

gap potential of d-CeO₂ as compared to p-CeO₂ attributed to the formation of new localized energy levels after the defect induction [18]. MCO-30 displayed a band gap potential value of 2 eV (Fig. S5c), showing the successful interaction between MIL-53 and d-CeO₂ [49]. The synergistic effect between MIL-53 and d-CeO₂ is deemed responsible for the reduced bandgap energy of MCO-30. Also, oxygen vacancies originating from CeO₂ are mainly accountable for the bandgap reduction. The reduction of Ce⁴⁺ ions to Ce³⁺ ions enable the formation of a large number of delocalized energy levels which can now serve as interband energy states for bandgap reduction in MCO-30 heterostructure [50]. Moreover, as proved by the XPS survey, since Fe is in a stable + 3 oxidation state (i.e. d5- half-filled) within the MCO-30 photocatalyst, the transition of electrons from Fe 3d to Ce 4f is considered highly unfavorable. Therefore, the occurrence of oxygen vacancies as well as the Ce³⁺ mediated intermediary defect states hinder the direct transition from O 2p to Ce 4f, concurrently resulting in a band gap reduction of the hybrid photocatalyst MCO-30 [51]. In context to the above, from the UV-Vis DRS analysis, it was established that MCO-30 exhibits absorption of visible light at a longer wavelength (619 nm) than pure MIL-53 (433 nm) and d-CeO₂ (441 nm). These results confirm that the formation of MCO-30 heterojunctions expanded the absorption edge toward the visible-light region. [52].

PL spectroscopy was used to determine the rate of recombination of the electrons and holes created by the irradiation of light. Reduced photocatalytic effectiveness is caused by increased emitted radiation and increased recombination, which leads to less electron-hole separation [53]. In contrast to pristine MIL-53, p-CeO₂, and d-CeO₂ (Fig. 6(c)), the emission spectral intensity of MCO-30 is relatively exceptionally low, demonstrating higher electron-hole separation and less recombination in MCO-30 heterostructure. Enhanced electron and hole separation in MCO-30 compound results in greater photocatalytic activity.

Electrochemical impedance spectroscopy (EIS) was used to quantify the charge transfer ability and interfacial charge recombination, and the results are shown in Fig. 7(a). Generally, a smaller semi-circle arc in the EIS Nyquist plot in a semiconductor material denotes a significant charge mobilization efficiency and lower charge transfer resistance [54]. In the Nyquist plot, MCO-30 heterostructure displays the shortest radius of the semicircle when compared to MIL-53, p-CeO₂ and d-CeO₂, which indicates high surface reaction kinetics could be achieved by MCO-30. To determine the exact flat band potential (E_{fb}) and the type of semi conductivity of the pristine materials, the Mott-Schottky analysis was carried out and the value of E_{fb} was calculated by using the well-known Mott-Schottky equation [55].

$$\frac{1}{C_s^2} = \frac{2}{N_D \xi \xi_0 e A^2} \left(V - E_{fb} - \frac{kT}{e} \right) \quad (5)$$

Where C_s= space charge capacitance, V = applied potential, E_{fb}=flat-band potential, k = Boltzmann constant (J/K), T = absolute temperature (K), N_D= donor density (cm⁻³), 'e' represents the electric charge (C), A = area (cm²) and finally ξ and ξ_0 represents dielectric constant of the semiconductor and vacuum permittivity. The diagram of 1/C_s² vs. V was extrapolated to the abscissa to determine the value of E_{fb}. MIL-53 and d-CeO₂ are both shown to have positive slopes in Fig. 7(b & c), indicating that they are both n-type semiconductors. MIL-53 and d-CeO₂ were found to have E_{fb} values of -0.73 eV and -0.44 eV (vs. Ag/AgCl), respectively. Similarly, p-CeO₂ shows the E_{fb} value of -0.64 eV (Fig. S6). Furthermore, the E_{fb} (vs. Ag/AgCl) of MIL-53, d-CeO₂, and p-CeO₂ may be changed to E_{fb} (vs. NHE) by using the formula E_{fb} (vs. NHE) = E_{fb} (vs. Ag/AgCl) + 0.197 [56]. After conversion, the E_{fb} values for MIL-53 and d-CeO₂ vs. NHE were -0.53 eV and -0.24 eV, respectively. Similarly, E_{fb} value for the p-CeO₂ was found to be -0.44 eV vs NHE. Typically, the n-type semiconductor's conduction band (CB) is

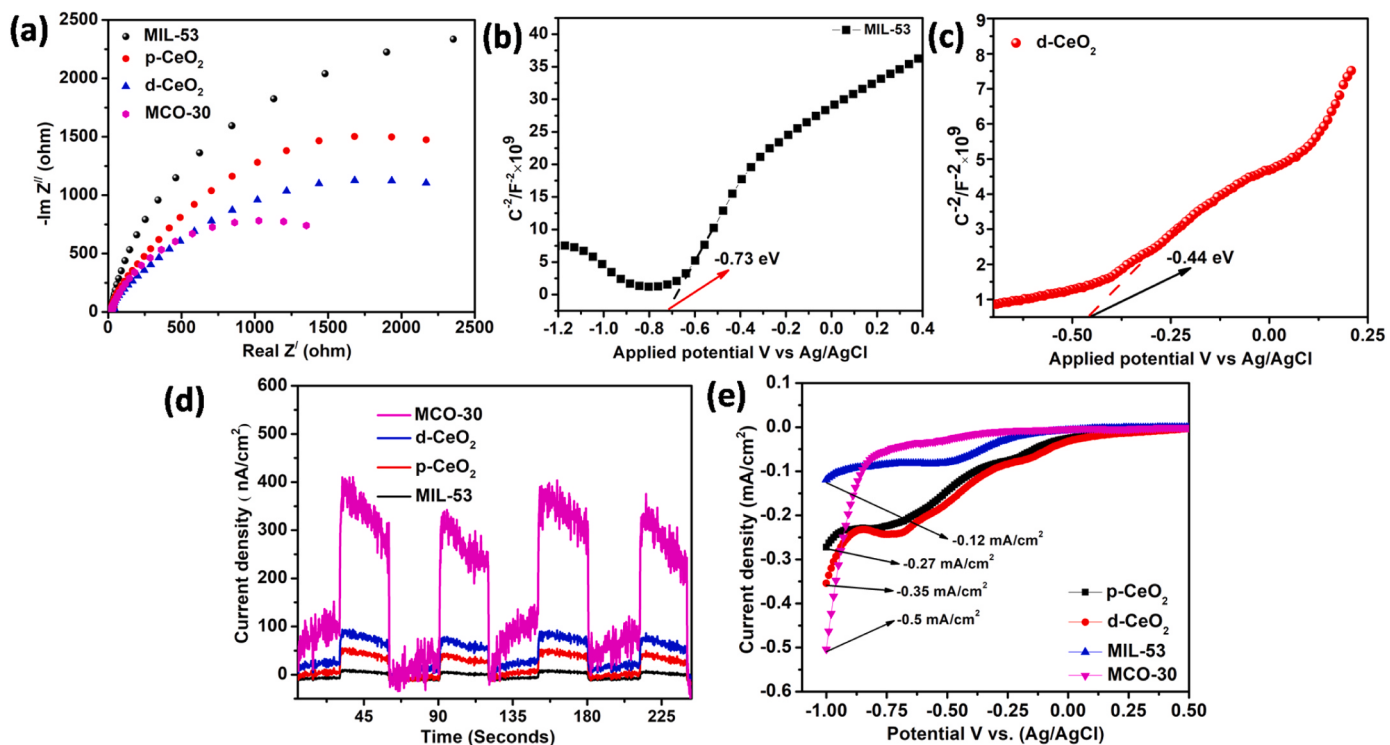


Fig. 7. (a) EIS Nyquist plot of MIL-53, p-CeO₂, d-CeO₂, and MCO-30 (b) MS plot of MIL-53 (c) MS plot of d-CeO₂ (d) Transient photocurrent study of MIL-53, p-CeO₂, d-CeO₂, and MCO-30 (e) LSV plot of MIL-53, d-CeO₂, and MCO-30.

0.1 eV lower than E_{fb} , while the p-type semiconductor's valence band (VB) is 0.1 eV higher than E_{fb} . [56]. The CB of MIL-53, p-CeO₂ and d-CeO₂ were -0.63 , -0.54 and -0.34 eV, respectively. The corresponding VB were obtained by the following equation.

$$E_g = E_{\text{VB}} - E_{\text{CB}} \quad (6)$$

Where E_g = Band gap energy, E_{VB} = Valence band edge potential, and E_{CB} = Conduction band edge potential. The VB for MIL-53, p-CeO₂ and d-CeO₂ were calculated to be 2.23 eV, 2.12 eV and 2.26 eV respectively.

The transient photocurrent response of pure MIL-53, p-CeO₂, d-CeO₂ and MCO-30 composite are presented in Fig. 7(d). When compared to other pristine materials, the MCO-30 heterostructure showed a substantial rise in current density, which suggests that the MCO-30 composite exhibits extraordinary charge separation and limited recombination. This significant charge separation between the electron and hole produced by the light is what accounts for the significant improvement of optoelectronic characteristics of MCO-30. The photocurrent study provides full support for both the PL and the electrochemical impedance (EIS) studies.

One of the most important techniques for measuring the current density and interfacial charge separation at the electrode-electrolyte interface in illuminated circumstances is linear sweep voltammetry (LSV). The MIL-53 and p-CeO₂ display a very minimum cathodic photocurrent (-0.12 mA.cm^{-2}) and (-0.27 mA.cm^{-2}), suggesting vulnerable adsorption of visible light by MIL-53 and p-CeO₂ (Fig. 7(e)). However, compared to p-CeO₂, defect-induced CeO₂ (d-CeO₂) showed a considerable increase in cathodic current (-0.35 mA.cm^{-2}), indicating improved electron hole separation following the creation of the oxygen vacancy in p-CeO₂. Additionally, MCO-30 exhibits cathodic photocurrent of -0.5 mA.cm^{-2} at the same applied potential of $-1.00 \text{ V vs. Ag/AgCl}$. MCO-30 has a cathodic photocurrent that is roughly four times higher than pure MIL-53 and 1.5 times higher than d-CeO₂. This shows that the electron channelization increases and the rate of charge pair exchange decreases after the heterojunction between d-CeO₂ and MIL-53 is formed.

The larger electrochemical active surface area (ECSA) of the as-synthesized photocatalyst served as additional confirmation of its high catalytic activity. The typical CV approach estimates a certain potential window in which the faradaic current response is small. Presumably, the current detected in this area is a charging current resulting from double-layer charging. On the other hand, the electrochemical double-layer capacitance (C_{dl}), which results from an interfacial charging process, is linearly related to ECSA [17,57]. The charging current and scan rate were plotted against a certain potential window (0.10 V vs. Ag/AgCl to 0.22 V vs. Ag/AgCl), yielding a straight line whose slope equaled twice the double-layer capacitance (C_{dl}), which equals the ECSA (Fig. S7). The primary way to assess ECSA alternatively is through direct correlation between the C_{dl} value and ECSA. The ECSA value of MCO-30 was found to be $0.000178 \text{ mF.cm}^{-2}$ which is higher as compared to MIL-53 ($0.000059 \text{ mF.cm}^{-2}$) and d-CeO₂ ($0.000166 \text{ mF.cm}^{-2}$). Upon normalizing the LSV curves using the electrochemical surface area (ECSA) to eliminate the impact of greater ECSA on HER performance, the findings presented in Fig. S7 (f) indicates HER activity is higher in MCO-30 than in MIL-53 as well as d-CeO₂. This demonstrates that the improved HER activity is connected to both the elevated ECSA and the enhanced intrinsic activity of the catalyst as a result of the refined electronic structure [57]. The turnover frequency (TOF) of the fabricated nanocomposite as well as its corresponding precursors has been calculated (Table S1). As depicted from the table, TOF of MCO-30 (0.155 s^{-1}) is comparatively higher than MIL-53 (0.012 s^{-1}) and d-CeO₂ (0.147 s^{-1}) indicating the higher catalytic efficiency of MCO-30 heterostructure.

5. Photocatalytic activity

5.1. Photocatalytic Bisphenol A degradation

In this research, visible light illumination ($\lambda > 400 \text{ nm}$) was used to decompose BPA using fabricated pure and heterostructure photocatalyst materials. Prior to the photodegradation process, the catalysts present

BPA solution was agitated in the dark for 1 h to achieve adsorption-desorption equilibrium. The influence of adsorption on the removal of BPA by different prepared catalysts is depicted in Fig. S8, which demonstrates that adsorption had a negligibly small effect on BPA removal. The deterioration process was then started by exposing the light to the reaction mixture containing catalyst. When there was no photocatalyst present, the breakdown of BPA was very minimal. When different manufactured catalysts were used, the rate of BPA breakdown significantly increased (Fig. 8(a)). The poor photocatalytic activity of d-CeO₂ (39%) and MIL-53 (16%) is shown by the degradation of BPA by these substances. However, the photodegradation of BPA was noticeably improved when MCO-X compounds were utilized in the degradation process. MCO-30 exhibits the highest photocatalytic activity when compared to all other compounds. Within 60 min of exposure to visible light, about 99% of BPA was degraded. Interestingly p-CeO₂ and 30% p-CeO₂ modified with MIL-53 (MPCO-30) shows the degradation activity of only 34% and 59% respectively (Fig. S9). Fig. S10 shows the UV-visible absorbance spectra of BPA adsorption and degradation by MCO-30. MCO-30 exhibits considerably higher photocatalytic activity than MPCO-30, indicating that Type-I charge transfer dynamics changed to Type-II once oxygen vacancy is induced in CeO₂. The significant separation of photo-induced electron-hole pairs in MCO-30 may be the result of this switching in charge transfer dynamics. Additionally, the results are considerably superior to some published research. (Table S2). The following equation, which assumes that all reactions take place via a pseudo-first-order process, was used to linearly match the experimental results for the comparative analysis (Fig. 8(b)).

$$\ln\left(\frac{C_0}{C_t}\right) = kt \quad (7)$$

Where k represents the rate constant (min^{-1}), C_0 and C_t represents the initial and final concentrations at time t of BPA pollutant.

For various synthesized photocatalysts, the rate constant (k) was calculated and shown in (Fig. 8(c)). It was found that the rate constant (k) for the MCO-30 compound was 0.045 min^{-1} , 5.25 times higher than that of MIL-53 (0.004 min^{-1}) and 5 times higher than that of d-CeO₂ (0.009 min^{-1}). The capacity of MCO-30 to be reused was tested for BPA degradation up to the fifth cycle (Fig. 8(d)). After the fifth cycle, the MCO-30 composite displays 95.5% degradation efficiency, demonstrating that it still possesses remarkable photo-produced hole and electron separation capabilities. The intermediate product created during the breakdown of bisphenol A was obtained using LC-MS analysis (Fig. S12), and based on the results, a probable reaction pathway was also displayed in Fig. S13.

5.2. Photocatalytic hydrogen evolution

Under visible light illumination, the photocatalytic H₂ generation efficacy of the acquired photocatalysts was examined using methanol as the scavenger reagent. The time-dependent hydrogen output using the MIL-53, d-CeO₂, and MCO-X heterostructure is shown in Fig. 9(a). It is evident that when exposed to visible light, pure MIL-53 almost completely fails to generate hydrogen, primarily due to the rapid recombination of photoinduced e-/h+ couples. It's interesting to note that MCO-X composites produce significantly more hydrogen, which suggests that the separation and movement efficacy of photo-generated carriers is significantly improved in MCO-X composites. The calculated average hydrogen evolution rate for the various samples is depicted in Fig. 9(b). It demonstrates that, when compared to pure MIL-53 and d-CeO₂, the hydrogen generation rate of MCO-X compounds is quite high. Among various MCO-X heterostructure, the hydrogen production rate of

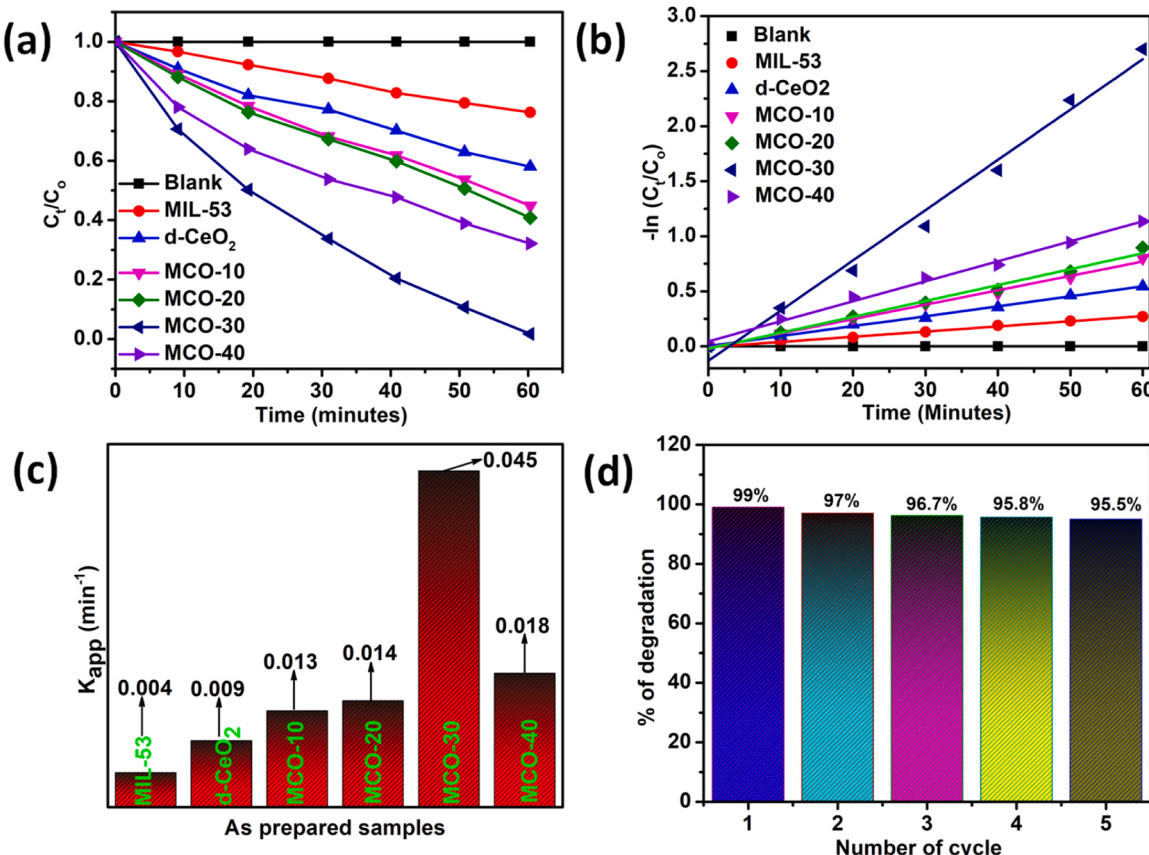


Fig. 8. (a) Photo-degradation of BPA by MIL-53, d-CeO₂, and MCO-X heterostructure (b) First-order kinetics for BPA degradation, (c) Rate constant of the materials for BPA degradation. (d) Recyclability plot for MCO-30 heterostructure.

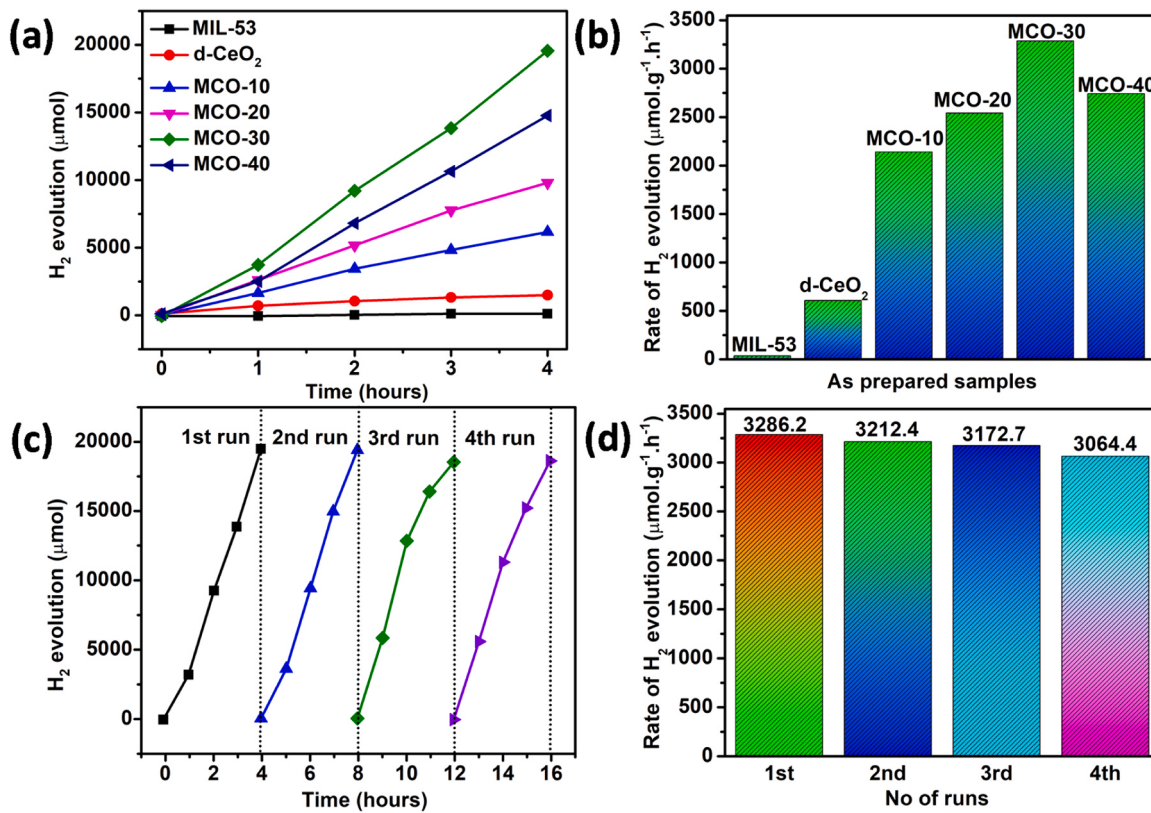


Fig. 9. (a) Quantity of H₂ production with time by MIL-53, d-CeO₂, and MCO-X composites. (b) H₂ evolution rate of MIL-53, d-CeO₂, and MCO-X heterostructure. (c) Recyclability test of photocatalytic H₂ generation for MCO-30 heterostructure and (d) Rate of H₂ evolution in four different run by MCO-30 heterostructure.

MCO-30 was 3286.2 μmol h⁻¹ g⁻¹, which is approximately 5.4 times superior to d-CeO₂. The results are also noticeably significant than some published research (Table S3). In contrast to MCO-30, which produced 3286.2 μmol h⁻¹ g⁻¹ of photocatalytic hydrogen, MCO-40 produced only 2734 μmol h⁻¹ g⁻¹ of hydrogen. This reduction is probably due to a masking effect caused by the excessive quantity of d-CeO₂ that has been added to the surface of MIL-53, which may obstruct the incoming light and reduce the effectiveness of the photocatalytic hydrogen generation. The increased performance of photocatalytic H₂ production for MCO-X hybrids over pure MIL-53 demonstrates that d-CeO₂ is a useful cocatalyst that can greatly increase performance in practical uses. A very small quantity of photocatalytic hydrogen generation is demonstrated by p-CeO₂ (358.92 μmol h⁻¹ g⁻¹) and MPCO-30 (922.74 μmol h⁻¹ g⁻¹) (Fig. S11). Stability, in addition to the capacity to produce H₂, is crucial for practical implementation. The reusability of the optimized sample (MCO-30) was evaluated using similar testing conditions. As per the

results (Fig. 9c and d), the hydrogen production effectiveness of MCO-30 does not show noteworthy reduction even after fourth run.

In the photodegradation process of BPA, various reactive species like e⁻, h⁺, ·O₂, and OH⁻ plays the most crucial role. To determine the influence of various active species, scavenger experiments are performed by using DMSO, EDTA, TBA, and p-BQ as electron (e⁻), hole (h⁺), hydroxyl radical (OH⁻), and superoxide radical (·O₂) scavengers, respectively (Fig. 10(a)). We have performed photocatalytic BPA degradation using several scavenger solutions (1 mM) in order to figure out the primary active species that are involved in the photocatalytic degradation process. Upon applying EDTA and TBA as hole and hydroxyl radical scavenger, the degradation of BPA was significantly decreased to 12% and 27%, signifies both hole and hydroxyl radical plays crucial role in the degradation process. However, with the addition of (p-BQ) and DMSO as superoxide radical and electron scavenger, then the degradation of BPA was 57% and 98%, signifies minimal effect of electron in the

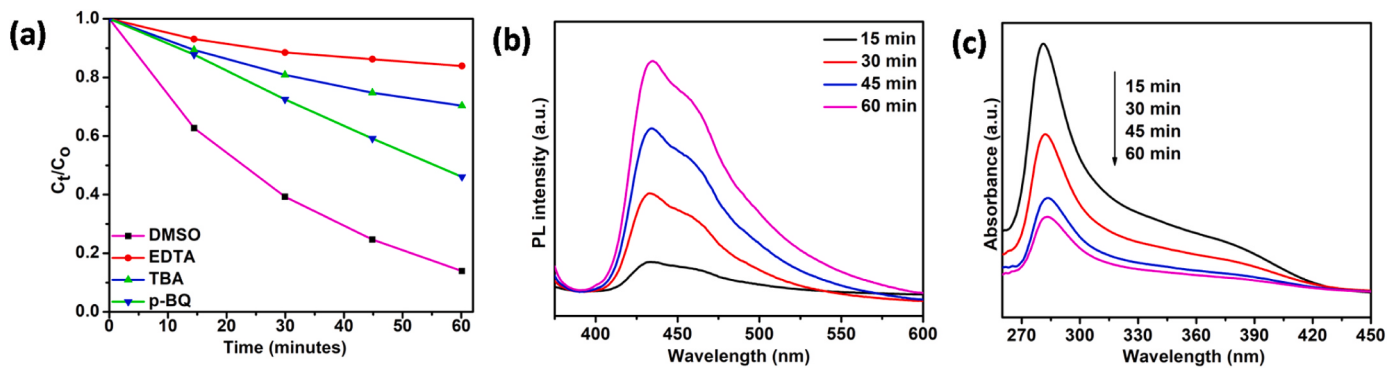


Fig. 10. (a) Trapping experiment for BPA degradation (b) Fluorescence profiles of 2-hydroxy terephthalic acid produced by aqueous solution of MCO-30 heterostructure at various irradiation intervals (c) NBT decrease rate as a function of time in the MCO-30 heterostructure.

degradation process. The effect of scavengers in the degradation process is in the order $\text{h}^+ > \text{OH}^- > \text{O}_2^- > \text{e}^-$.

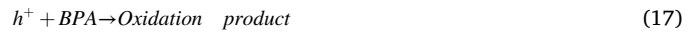
To further assess the production of O_2^- radical and OH^- radical, reactive radical trapping tests are conducted in the aqueous photocatalyst solution. To study how hydroxyl radicals (OH^-) arise, the terephthalic acid photoluminescence probing technique (TA-PL) was carried out (Fig. 10(b)), whereas superoxide radicals (O_2^-) formation is investigated using nitroblue tetrazolium chloride (NBT) as probe molecule via UV-vis spectroscopy (Fig. 10(c)) [58]. According to the literature, the powerful oxidant hydroxyl radical ($\bullet\text{OH}$) reacts with terephthalic acid to produce the extremely fluorescent 2-hydroxy terephthalic acid (HTA). A PL emission band at about 425 nm verifies the synthesis of HTA during the reaction, which ultimately confirms the generation of the hydroxyl radical ($\bullet\text{OH}$) [34]. The formation of $\bullet\text{OH}$ in MCO-30 heterostructure is confirmed by the steady enhancement in PL intensity of the MCO-30 aqueous solution as the illumination period increases (Fig. 10(b)). Typically, the hydroxyl radical is created by either the direct oxidation of VB hole or by the indirect multistep reduction of dissolved oxygen by the photoexcited electrons. Since the valence band potential of MIL-53 in MCO-30 heterostructure is (2.23 eV vs. NHE) which is quite enough to form hydroxyl radical $\text{OH}^- / \bullet\text{OH}$ (1.99 eV vs. NHE) [34]. Furthermore, the NBT test was carried out using UV-vis spectroscopy to verify the generation of superoxide radicals ($\bullet\text{O}_2^-$). The molecular absorption peak of NBT is at 280 nm, and its intensity continuously decreases when it reacts with ($\bullet\text{O}_2^-$) radicals by creating formazan derivatives [31]. It is evident from Fig. 10(c), that the absorbance maxima at 280 nm constantly diminish, suggesting that the superoxide radicals ($\bullet\text{O}_2^-$) is continuously trapped and forms formazan derivatives. Accordingly, it can be inferred from the above findings that vigorous superoxide radicals ($\bullet\text{O}_2^-$) also develop in the aqueous solution of MCO-30 heterostructure.

Recycling tests were done on photocatalytic BPA breakdown (Fig. 8 (d)) and H_2 generation (Fig. 9(c)) up to the fourth cycle to see if the synthesized MCO-30 heterostructure could be recycled. The photocatalyst is recycled after every cycle through centrifugation, washing, and drying at 60 °C. The effectiveness of the photocatalyst dropped to an extremely small degree after the fifth catalytic cycle. The mass loss of the MCO-30 photocatalyst during the recycling procedure is the likely cause of the decline in effectiveness. The photocatalyst (MCO-30) used in this experiment was studied using XRD and SEM, and the results are shown in Fig. 11. There are no discernible changes in the crystallinity or morphology of the photocatalyst, indicating that it can maintain its structural integrity throughout the BPA breakdown process.

6. Possible photocatalytic mechanism

Based on the aforementioned observations, a potential mechanism that could explain the switching of charge transfer in MCO-30 following the defect creation in CeO_2 was predicted. Both CeO_2 and MIL-53 exhibited the beneficial band alignment, which is essential for the

efficient photoinduced charge separation and their mobilization. The mott-schottkey and band gap energy analysis revealed that the valence band (VB) positions of MIL-53 and p-CeO_2 were 2.23 and 2.12 eV, respectively, and that their respective conduction (CB) bands were – 0.63 and – 0.54 eV. The photo induced electrons travel from the CB of MIL-53 to p-CeO_2 upon exposure to light, whereas the corresponding holes move from the VB of MIL-53 to p-CeO_2 . This kind of charge flow has a tendency to favor Type-I mechanisms over other types of charge transfer mechanisms and exhibits low photocatalytic effectiveness due to the high chance of recombination of photoinduced charge couples. However, due to the development of a new localized energy level in CeO_2 , d-CeO_2 exhibited its corresponding VB and CB to be 2.26 and – 0.34 eV, respectively. As a result, when oxygen vacancy-mediated CeO_2 (d-CeO_2) and MIL-53 couple, charge transfer occurs via a Type-II mechanism in which photo excited electrons move from the CB of MIL-53 to the CB of d-CeO_2 and the corresponding holes move from the VB of d-CeO_2 to the VB of MIL-53. According to literature, Type-II charge transfer mechanisms are more effective than Type-I charge transfer mechanisms in terms of photocatalytic efficiency since the chance of charge pair recombination is much lower in Type-II than Type-I [59]. The oxygen vacancy in p-CeO_2 is the cause of the switching of charge transfer dynamics in the MCO-30 heterostructure, which significantly increases photocatalytic activity in BPA degradation and hydrogen generation from water splitting. The following equations describe the precise photocatalytic mechanism.



7. Conclusions

This work reports the fabrication of heterojunction between defect induced CeO_2 (d-CeO_2)/ MIL-53 for expeditious photodegradation of BPA and H_2 generation from water splitting. Oxygen vacancy mediated

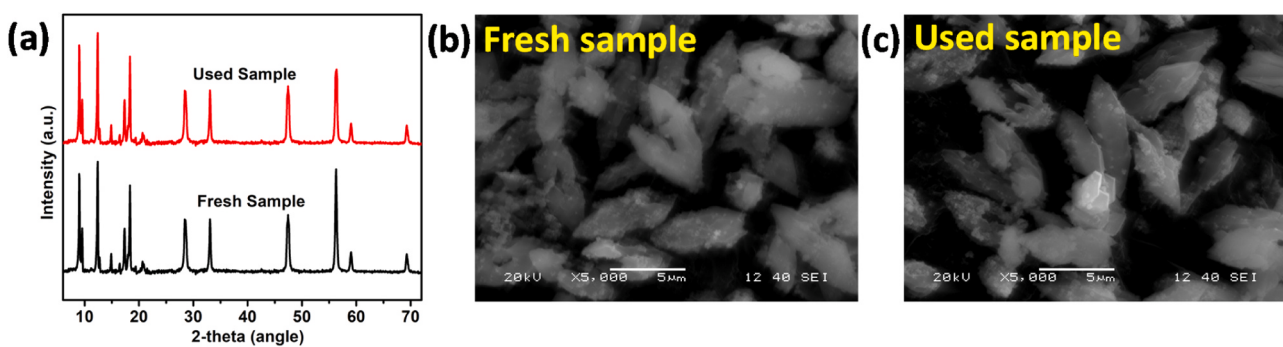


Fig. 11. (a) XRD pattern of MCO-30 heterostructure before and after the photocatalytic reaction. (b) SEM image of MCO-30 heterostructure before photocatalytic application. (c) SEM image of MCO-30 composite after photocatalytic application.

CeO_2 can switch the charge transfer dynamics from Type-I to Type-II in MCO-30 heterostructure. MCO-30 exhibits outstanding photocatalytic activity, since this switching in charge transfer enhances the separation of photoinduced charge couples and minimizes the recombination. The optimal photocatalyst (MCO-30) exhibits significant photocatalytic performances towards BPA degradation (99%) and H_2 evolution (3286.2 $\mu\text{mol h}^{-1} \text{g}^{-1}$) which is remarkably high than that of pure CeO_2 and MIL-53, respectively. Radical trapping experiments suggested the vigorous formation of reactive superoxide radical ($\bullet\text{O}_2^-$) and hydroxyl radical ($\bullet\text{OH}$) in aqueous suspension of the MCO-30 heterostructure. The pivotal role of ($\bullet\text{O}_2^-$) and ($\bullet\text{OH}$) has been described towards degradation of BPA. This work furnishes a way to fabricate oxygen vacancy induced CeO_2 mediated with MIL-53 which can switch the photoinduced charge transfer mechanism from Type-I to Type-II to enhance the photocatalytic effectiveness in BPA degradation and H_2 evolution. This heterostructure can be used as a prospective contender in the fields of producing renewable energy sources and cleaning up persistent organic contaminants.

CRediT authorship contribution statement

Ugrabadi Sahoo: Conceptualization, Investigation, Methodology, Results analysis, Writing – original draft. **Samarjit Pattnayak:** Data Curation, Visualization. **Shubhalaxmi Choudhury:** Visualization. **Pragnyashree Aparajita:** Conceptualization, Formal analysis. **Dillip Kumar Pradhan:** Conceptualization, Validation. **Garudadhwaj Hota*** : Supervision, Validation, Funding acquisition, Writing – review & editing.

Declaration of Competing Interest

The authors declare that they have no known competing financial interests or personal relationships that could have appeared to influence the work reported in this paper.

Data Availability

No data was used for the research described in the article.

Acknowledgment

The author acknowledges NIT Rourkela in Odisha, India for providing the research infrastructure needed to complete this study and University of Grants Commission (UGC) for providing financial assistance.

Associated content

None.

Supporting Information Available

XRD, FTIR, Elemental mapping, EPR, EDX analysis, Tauc's plot, UV visible absorbance plot, Mott- Schottky plot, LC-MS, and conversion efficiency for H_2 evolution are presented in the supporting information file.

Appendix A. Supporting information

Supplementary data associated with this article can be found in the online version at [doi:10.1016/j.apcatb.2023.123524](https://doi.org/10.1016/j.apcatb.2023.123524).

References

- Y. Yeom, J. Han, X. Zhang, C. Shang, T. Zhang, X. Li, X. Duan, D.D. Dionysiou, A review on the degradation efficiency, DBP formation, and toxicity variation in the UV/chlorine treatment of micropollutants, *Chem. Eng. J.* 424 (2021), 130053, <https://doi.org/10.1016/j.cej.2021.130053>.
- Q.Y. Wu, Z.W. Yang, Y. Du, W.Y. Ouyang, W.L. Wang, The promotions on radical formation and micropollutant degradation by the synergies between ozone and chemical reagents (synergistic ozonation): a review, *J. Hazard. Mater.* 418 (2021), <https://doi.org/10.1016/j.jhazmat.2021.126327>.
- X. Li, N. Li, Y. Gao, L. Ge, Design and applications of hollow-structured nanomaterials for photocatalytic H_2 evolution and CO_2 reduction, *Chin. J. Catal.* 43 (2022) 679–707, [https://doi.org/10.1016/S1872-2067\(21\)63863-9](https://doi.org/10.1016/S1872-2067(21)63863-9).
- R. Mohanty, S. Mansingh, K. Parida, K. Parida, Boosting sluggish photocatalytic hydrogen evolution through piezo-stimulated polarization: a critical review, *Mater. Horiz.* 9 (2022) 1332–1355, <https://doi.org/10.1039/d1mh01899j>.
- J. Xing, S. Zhang, M. Zhang, J. Hou, A critical review of presence, removal and potential impacts of endocrine disruptors bisphenol A, *Comp. Biochem. Physiol. Part - C. Toxicol. Pharmacol.* 254 (2022), 109275, <https://doi.org/10.1016/j.cbpc.2022.109275>.
- P.V.L. Reddy, K.H. Kim, B. Kavitha, V. Kumar, N. Raza, S. Kalagara, Photocatalytic degradation of bisphenol A in aqueous media: a review, *J. Environ. Manag.* 213 (2018) 189–205, <https://doi.org/10.1016/j.jenvman.2018.02.059>.
- Y.M. Hunge, A.A. Yadav, S. Khan, K. Takagi, N. Suzuki, K. Teshima, C. Terashima, A. Fujishima, Photocatalytic degradation of bisphenol A using titanium dioxide@ nanodiamond composites under UV light illumination, *J. Colloid Interface Sci.* 582 (2021) 1058–1066, <https://doi.org/10.1016/j.jcis.2020.08.102>.
- S.W. Lv, J.M. Liu, C.Y. Li, N. Zhao, Z.H. Wang, S. Wang, Two novel MOFs@COFs hybrid-based photocatalytic platforms coupling with sulfate radical-involved advanced oxidation processes for enhanced degradation of bisphenol A, *Chemosphere* 243 (2020), 125378, <https://doi.org/10.1016/j.chemosphere.2019.125378>.
- G. Li, C. Yang, Q. He, J. Liu, Ag-based photocatalytic heterostructures: construction and photocatalytic energy conversion application, *J. Environ. Chem. Eng.* 10 (2022), 107374, <https://doi.org/10.1016/j.jece.2022.107374>.
- S. Song, Z. Xing, H. Zhao, Z. Li, Wei Zhou, Recent advances in bismuth-based photocatalysts: environment and energy applications, *Green. Energy Environ.* (2022), <https://doi.org/10.1016/j.gee.2022.04.004>.
- D. Ayodhya, Semiconductors-based Z-scheme materials for photoelectrochemical water splitting: a review, *Electrochim. Acta* 448 (2023), 142118, <https://doi.org/10.1016/j.electacta.2023.142118>.
- J. Chen, N. Kang, J. Fan, C. Lu, K. Lv, Carbon nitride for photocatalytic water splitting to produce hydrogen and hydrogen peroxide, *Mater. Today Chem.* 26 (2022), 101028, <https://doi.org/10.1016/j.mtchem.2022.101028>.
- A.A. Fauzi, A.A. Jalil, N.S. Hassan, F.F.A. Aziz, M.S. Azami, I. Hussain, R. Saravanan, D.V.N. Vo, A critical review on relationship of CeO_2 -based photocatalyst towards mechanistic degradation of organic pollutant, *Chemosphere* 286 (2022), <https://doi.org/10.1016/j.chemosphere.2021.131651>.
- T. Kaur, R. Kumar, S. Khan, K. Singh, J. Kolte, Structural and electrical properties of Gd doped CeO_2 (GDC) nanoceramics for solid oxide fuel cell applications, *Trans. Indian Ceram. Soc.* 81 (2022) 127–132, <https://doi.org/10.1080/0371750X.2022.2115400>.
- W. Zhang, X. Wang, J. Wu, X. Wang, X. Lv, G. Liu, B. Li, J. Zhou, E. Xie, Z. Zhang, Electrospun Nb-doped CeO_2 nanofibers for humidity independent acetone sensing, *Appl. Surf. Sci.* 602 (2022), 154303, <https://doi.org/10.1016/j.apsusc.2022.154303>.
- S.N. Matussin, M.H. Harunsani, M.M. Khan, CeO_2 and CeO_2 -based nanomaterials for photocatalytic, antioxidant and antimicrobial activities, *J. Rare Earths* 41 (2022), <https://doi.org/10.1016/j.jre.2022.09.003>.
- S. Zhao, Y. Yang, Z. Tang, Insight into structural evolution, active sites, and stability of heterogeneous electrocatalysts, *Angew. Chem. - Int. Ed.* 61 (2022), <https://doi.org/10.1002/anie.202110186>.
- M.M. Khan, S.A. Ansari, D. Pradhan, D.H. Han, J. Lee, M.H. Cho, Defect-induced band gap narrowed CeO_2 nanostructures for visible light activities, *Ind. Eng. Chem. Res.* 53 (2014) 9754–9763, <https://doi.org/10.1021/ie500986n>.
- X. Lu, D. Zheng, P. Zhang, C. Liang, P. Liu, Y. Tong, Facile synthesis of free-standing CeO_2 nanorods for photoelectrochemical applications, *Chem. Commun.* 46 (2010) 7721–7723, <https://doi.org/10.1039/c0cc01854f>.
- Y. Wang, Z. Liu, R. Wang, NaBH_4 Surface Modification on CeO_2 Nanorods Supported Transition-Metal Catalysts for Low Temperature CO Oxidation, *ChemCatChem* 12 (2020) 4304–4316, <https://doi.org/10.1002/cctc.202000789>.
- W. Gao, Z. Zhang, J. Li, Y. Ma, Y. Qu, Surface engineering on CeO_2 nanorods by chemical redox etching and their enhanced catalytic activity for CO oxidation, *Nanoscale* 7 (2015) 11686–11691, <https://doi.org/10.1039/c5nr01846c>.
- Y. Wang, L. Zhao, J. Ma, J. Zhang, Confined interface transformation of metal-organic frameworks for highly efficient oxygen evolution reactions, *Energy Environ. Sci.* 15 (2022) 3830–3841, <https://doi.org/10.1039/d2ee01073a>.
- R. Abazari, A.R. Mahjoub, J. Sharifi, Synthesis of a nanostructured pillar MOF with high adsorption capacity towards antibiotics pollutants from aqueous solution, *J. Hazard. Mater.* 366 (2019) 439–451, <https://doi.org/10.1016/j.jhazmat.2018.12.030>.
- L. Wang, M. Zheng, Z. Xie, Nanoscale metal-organic frameworks for drug delivery: A conventional platform with new promise, *J. Mater. Chem. B* 6 (2018) 707–717, <https://doi.org/10.1039/c7tb02970e>.
- B. Yan, Photofunctional MOF-based hybrid materials for the chemical sensing of biomarkers, *J. Mater. Chem. C* 7 (2019) 8155–8175, <https://doi.org/10.1039/c9tc01477b>.
- Y. Zhang, X. Yang, H.C. Zhou, Synthesis of MOFs for heterogeneous catalysis via linker design, *Polyhedron* 154 (2018) 189–201, <https://doi.org/10.1016/j.poly.2018.07.021>.

[27] W. Zeng, T. Cai, Y. Liu, L. Wang, W. Dong, H. Chen, X. Xia, An artificial organic-inorganic Z-scheme photocatalyst $\text{WO}_3@\text{Cu@PDI}$ supramolecular with excellent visible light absorption and photocatalytic activity, *Chem. Eng. J.* 381 (2020), 122691, <https://doi.org/10.1016/j.cej.2019.122691>.

[28] K. Khaletskaya, A. Pougin, R. Medishetty, C. Rösler, C. Wiktor, J. Strunk, R. Fischer, Fabrication of Gold/Titania Photocatalyst for CO_2 Reduction Based on Pyrolytic Conversion of the Metal-Organic Framework $\text{NH}_2\text{-MIL-125(Ti)}$ Loaded with Gold Nanoparticles, *Chem. Mater.* 27 (2015) 7248–7257, <https://doi.org/10.1021/acs.chemmater.5b03017>.

[29] Y. Liu, J. Zhang, L. Song, W. Xu, Z. Guo, X. Yang, X. Wu, X. Chen, Au-HKUST-1 composite nanocapsules: Synthesis with a coordination replication strategy and catalysis on CO oxidation, *ACS Appl. Mater. Interfaces* 8 (2016) 22745–22750, <https://doi.org/10.1021/acsami.6b06209>.

[30] L. He, Y. Dong, Y. Zheng, Q. Jia, S. Shan, Y. Zhang, A novel magnetic $\text{MIL-101(Fe)}/\text{TiO}_2$ composite for photo degradation of tetracycline under solar light, *J. Hazard. Mater.* 361 (2019) 85–94, <https://doi.org/10.1016/j.jhazmat.2018.08.079>.

[31] U. Sahoo, S. Pattnayak, S. Choudhury, S. Padhia, M. Tripathy, G. Hota, Silver-nanoparticle-decorated $\text{g-C}_3\text{N}_4/\text{MIL-53(Fe)}$ nanocomposites: a pre-eminent visible-light-driven photocatalyst toward multimodal photocatalytic applications, *Ind. Eng. Chem. Res.* 61 (2022) 9703–9716, <https://doi.org/10.1021/acs.iecr.2c01819>.

[32] N.C. Zheng, Z. Wang, J.Y. Long, L.J. Kong, D.Y. Chen, Z.Q. Liu, Shape-dependent adsorption of CeO_2 nanostructures for superior organic dye removal, *J. Colloid Interface Sci.* 525 (2018) 225–233, <https://doi.org/10.1016/j.jcis.2018.03.087>.

[33] R. Bariki, D. Majhi, K. Das, A. Behera, B.G. Mishra, Facile synthesis and photocatalytic efficacy of $\text{UiO-66/CdIn}_2\text{S}_4$ nanocomposites with flowerlike 3D-microspheres towards aqueous phase decontamination of triclosan and H_2 evolution, *Appl. Catal. B Environ.* 270 (2020), 118882, <https://doi.org/10.1016/j.apcatb.2020.118882>.

[34] U. Sahoo, S. Choudhury, S. Pattnayak, P. Aparajita, Strategic growth engineering of Ag self-doped Ag_2CO_3 on MIL-53 MOF : A novel p-n heterostructure facilitates serendipitous charge migration and remarkable multimodal photocatalytic activity, *Mater. Today Commun.* 35 (2023), 105842, <https://doi.org/10.1016/j.mtcomm.2023.105842>.

[35] A. Suguna, S. Prabhu, M. Selvaraj, M. Geerthana, A. Silambarasan, M. Navaneethan, R. Ramesh, C. Sridevi, Annealing effect on photocatalytic activity of ZnO nanostructures for organic dye degradation, *J. Mater. Sci. Mater. Electron.* 33 (2022) 8868–8879, <https://doi.org/10.1007/s10854-021-06942-y>.

[36] H. Chen, Y. Liu, T. Cai, W. Dong, L. Tang, X. Xia, L. Wang, T. Li, Boosting Photocatalytic Performance in Mixed-Valence MIL-53(Fe) by Changing $\text{Fe(II)}/\text{Fe(III)}$ Ratio, *ACS Appl. Mater. Interfaces* 11 (2019) 28791–28800, <https://doi.org/10.1021/acsami.9b05829>.

[37] B. Soni, S. Makkar, S. Biswas, Defects induced tailored optical and magnetic properties of Zn-doped CeO_2 nanoparticles synthesized by a facile sol-gel type process, *J. Alloy. Compd.* 879 (2021), 160149, <https://doi.org/10.1016/j.jallcom.2021.160149>.

[38] P.C.A. Brito, D.A.A. Santos, J.G.S. Duque, M.A. Macêdo, Structural and magnetic study of Fe-doped CeO_2 , *Phys. B Condens. Matter* 405 (2010) 1821–1825, <https://doi.org/10.1016/j.physb.2010.01.054>.

[39] S.K. Patra, S. Rahut, J.K. Basu, Enhanced Z-scheme photocatalytic activity of a π -conjugated heterojunction: $\text{MIL-53(Fe)}/\text{Ag/g-C}_3\text{N}_4$, *N. J. Chem.* 42 (2018) 18598–18607, <https://doi.org/10.1039/c8nj04080j>.

[40] W. Xiong, Z. Zeng, X. Li, G. Zeng, R. Xiao, Z. Yang, Y. Zhou, C. Zhang, M. Cheng, L. Hu, C. Zhou, L. Qin, R. Xu, Y. Zhang, Multi-walled carbon nanotube/amine-functionalized MIL-53(Fe) composites: Remarkable adsorptive removal of antibiotics from aqueous solutions, *Chemosphere* 210 (2018) 1061–1069, <https://doi.org/10.1016/j.chemosphere.2018.07.084>.

[41] D.T.C. Nguyen, H.T.N. Le, T.S. Do, V.T. Pham, D.L. Tran, V.T.T. Ho, T.Van Tran, D. C. Nguyen, T.D. Nguyen, L.G. Bach, H.K.P. Ha, V.T. Doan, Metal-Organic Framework MIL-53(Fe) as an adsorbent for ibuprofen drug removal from aqueous solutions: Response surface modeling and optimization, *J. Chem.* 2019 (2019), <https://doi.org/10.1155/2019/5602957>.

[42] M. Tripathy, S. Padhia, S. Kar, G. Hota, A.K. Ghosh, Hematite decorated functional porous graphitic carbon nitride binary nanohybrid: Mechanistic insight into the formation and arsenic adsorption study, *Appl. Surf. Sci.* 583 (2022), 152443, <https://doi.org/10.1016/j.apsusc.2022.152443>.

[43] A.P. Chernyshov, Oxygen vacancy concentration in nanoobjects of $\text{CeO}_2-\delta$: Effects of characteristic size, morphology, and temperature, *Mater. Chem. Phys.* 282 (2022), 125979, <https://doi.org/10.1016/j.matchemphys.2022.125979>.

[44] S. Zhao, C. Tan, C.T. He, P. An, F. Xie, S. Jiang, Y. Zhu, K.H. Wu, B. Zhang, H. Li, J. Zhang, Y. Chen, S. Liu, J. Dong, Z. Tang, Structural transformation of highly active metal-organic framework electrocatalysts during the oxygen evolution reaction, *Nat. Energy* 5 (2020) 881–890, <https://doi.org/10.1038/s41560-020-00709-1>.

[45] R. Abazari, A.R. Mahjoub, Amine-functionalized $\text{Al-MOF}@\text{yxSm}_2\text{O}_3\text{-ZnO}$: a visible light-driven nanocomposite with excellent photocatalytic activity for the photo-degradation of amoxicillin, *Inorg. Chem.* 57 (2018) 2529–2545, <https://doi.org/10.1021/acs.inorgchem.7b02880>.

[46] M. Wang, M. Shen, X. Jin, J. Tian, M. Li, Y. Zhou, L. Zhang, Y. Li, J. Shi, Oxygen vacancy generation and stabilization in CeO_2-x by Cu introduction with improved CO_2 photocatalytic reduction activity, *ACS Catal.* 9 (2019) 4573–4581, <https://doi.org/10.1021/acscatal.8b03975>.

[47] R. Bariki, Y.P. Bhoi, S.K. Pradhan, S. Panda, S.K. Nayak, K. Das, D. Majhi, B. G. Mishra, Oxygen defect rich $\text{Bi}_2\text{S}_3/\text{SnS}_2/\text{Bi}$ -self doped $\text{Bi}_2\text{W}_2\text{O}_9$ multijunction photocatalyst for enhanced degradation of methyl parathion and H_2 evolution, *Sep. Purif. Technol.* 324 (2023), 124509, <https://doi.org/10.1016/j.seppur.2023.124509>.

[48] J. Jiao, Y. Wei, Z. Zhao, J. Liu, J. Li, A. Duan, G. Jiang, Photocatalysts of 3D ordered macroporous TiO_2 -supported CeO_2 nanolayers: Design, preparation, and their catalytic performances for the reduction of CO_2 with H_2O under simulated solar irradiation, *Ind. Eng. Chem. Res.* 53 (2014) 17345–17354, <https://doi.org/10.1021/ie503333b>.

[49] W. He, L. Liu, T. Ma, H. Han, J. Zhu, Y. Liu, Z. Fang, Z. Yang, K. Guo, Controllable morphology $\text{CoFe}_2\text{O}_4/\text{g-C}_3\text{N}_4$ p-n heterojunction photocatalysts with built-in electric field enhance photocatalytic performance, *Appl. Catal. B Environ.* 306 (2022), 121107, <https://doi.org/10.1016/j.apcatb.2022.121107>.

[50] S. Singh Suman, A. Kumar Ankita, N. Kataria, S. Kumar, P. Kumar, Photocatalytic activity of $\alpha\text{-Fe}_2\text{O}_3/\text{CeO}_2$ and $\text{CeO}_2@\alpha\text{-Fe}_2\text{O}_3$ core-shell nanoparticles for degradation of Rose Bengal dye, *J. Environ. Chem. Eng.* 9 (2021), <https://doi.org/10.1016/j.jece.2021.106266>.

[51] A. Das, M. Patra, M. Kumar P, M. Bhagavathiachari, R.G. Nair, Defect-induced visible-light-driven photocatalytic and photoelectrochemical performance of ZnO-CeO_2 nanoheterojunctions, *J. Alloy. Compd.* 858 (2021), 157730, <https://doi.org/10.1016/j.jallcom.2020.157730>.

[52] Y. Li, Y. Fang, Z. Cao, N. Li, D. Chen, Q. Xu, J. Lu, Construction of $\text{g-C}_3\text{N}_4/\text{PDI}$ MOF heterojunctions for the highly efficient visible light-driven degradation of pharmaceutical and phenolic micropollutants, *Appl. Catal. B Environ.* 250 (2019) 150–162, <https://doi.org/10.1016/j.apcatb.2019.03.024>.

[53] R. Bariki, S. Kumar Pradhan, S. Panda, S. Kumar Nayak, D. Majhi, K. Das, B. G. Mishra, In-situ synthesis of structurally oriented hierarchical $\text{UiO-66-(NH}_2\text{)}/\text{CdIn}_2\text{S}_4/\text{CaIn}_2\text{S}_4$ heterostructure with dual S-scheme engineering for photocatalytic renewable H_2 production and asulam degradation, *Sep. Purif. Technol.* 314 (2023), 123558, <https://doi.org/10.1016/j.seppur.2023.123558>.

[54] S. Shoran, A. Sharma, S. Chaudhury, Visible light enhanced photocatalytic degradation of organic pollutants with $\text{SiO}_2/\text{g-C}_3\text{N}_4$ nanocomposite for environmental applications, *Environ. Sci. Pollut. Res.* (2023), <https://doi.org/10.1007/s11356-022-24837-1>.

[55] D. Majhi, K. Das, A. Mishra, R. Dhiman, B.G. Mishra, One pot synthesis of $\text{CdS}/\text{BiOBr}/\text{Bi}_2\text{O}_2\text{CO}_3$: a novel ternary double Z-scheme heterostructure photocatalyst for efficient degradation of atrazine, *Appl. Catal. B Environ.* 260 (2020), 118222, <https://doi.org/10.1016/j.apcatb.2019.118222>.

[56] H. Sun, P. Qin, Z. Wu, C. Liao, J. Guo, S. Luo, Y. Chai, Visible light-driven photocatalytic degradation of organic pollutants by a novel $\text{Ag}_3\text{VO}_4/\text{Ag}_2\text{CO}_3$ p-n heterojunction photocatalyst: Mechanistic insight and degradation pathways, *J. Alloy. Compd.* 834 (2020), 155211, <https://doi.org/10.1016/j.jallcom.2020.155211>.

[57] Y. Huang, L.W. Jiang, B.Y. Shi, K.M. Ryan, J.J. Wang, Highly efficient oxygen evolution reaction enabled by phosphorus doping of the Fe electronic structure in iron–nickel selenide nanosheets, *Adv. Sci.* 8 (2021) 1–7, <https://doi.org/10.1002/advs.202101775>.

[58] Q. Wang, K. Zhang, S. Zheng, X. Hu, L. Wang, H. Du, D. Hao, G. Yang, An innovative $\text{Ag}/\text{MIL-100(Fe)}$ Z-scheme heterojunction for simultaneously enhanced photoreduction of Cr(VI) and antibacterial activity, *Appl. Surf. Sci.* 616 (2023), 156528, <https://doi.org/10.1016/j.apsusc.2023.156528>.

[59] J. Yang, T. Liu, H. Zhou, W. Cao, C. Chen, X. He, C. Jiang, Y. Li, Y. Wang, In situ conversion of typical type-I $\text{MIL-125(Ti)}/\text{BiOBr}$ into type-II heterostructure photocatalyst via MOF self-sacrifice: photocatalytic mechanism and theoretical study, *J. Alloy. Compd.* 900 (2022), 163440, <https://doi.org/10.1016/j.jallcom.2021.163440>.